

Experimental determination of the density matrix describing collisionally produced $H(n=3)$ atoms

C. C. Havener,* N. Rouze,[†] W. B. Westerveld, and J. S. Risley

Department of Physics, North Carolina State University, Raleigh, North Carolina 27695-8202

(Received 7 January 1985)

An experimental technique and analysis procedure is described for determining the axially symmetric density matrix for collisionally produced $H(n=3)$ atoms by measuring the Stokes parameters which characterize the emitted Balmer- α radiation as a function of axial and transverse electric fields applied in the collision cell. The electric fields induce strong characteristic variations in the Stokes parameters. The 14 independent elements of the density matrix are determined by fitting the observed Stokes parameters with signals calculated from a theoretical analysis of the experiment. The physical interpretation of the density matrix is presented in terms of graphs of the electron probability distribution and the electron current distribution. Examples of the determination of the density matrix are given for 40-, 60-, and 80-keV $H^+ + He$ electron-transfer collisions.

I. INTRODUCTION

Recently, this laboratory has reported on an experimental measurement which showed that a large electric dipole moment is induced in $H(n=3)$ atoms formed in electron-transfer collisions^{1,2} and has determined, for the first time, the electron current distribution for the $H(n=3)$ atoms.³

The specific collision considered was



for collision energies of 40, 60, and 80 keV. In the collision experiment the Stokes parameters which characterized the Balmer- α radiation emitted from decaying $H(n=3)$ atoms were measured as a function of static electric fields applied within the collision cell. These fields were insufficient to affect the collisions but modified the time evolution of the excited atoms in a well-known manner. The Stokes parameters exhibited strong characteristic dependencies on the applied electric fields.

The electric-field-dependent Balmer- α signals can be analyzed using a density-matrix description of the hydrogen atoms. The density matrix provides the most general characterization of collisionally produced atoms. The diagonal elements when properly normalized are the cross sections for producing individual nlm_l sublevels and the off-diagonal elements account for the coherent production of different sublevels. As described below, the density matrix can be used to obtain the "electron probability distribution" and the "electron current distribution" within the excited atoms. These physically meaningful quantities illustrate the importance of measuring the complete density matrix for describing collisionally produced atoms.

This paper discusses in detail the experimental techniques and theoretical analysis which can be used to obtain the electric dipole moment, the electron current distribution, and the electron probability distribution. Emphasis is placed on the measurement of the complete density matrix including the individual cross sections and coherence terms.

The specific collision considered in this paper is one example of a wide range of collision processes involving electron transfer from various gas targets to an incident ion. This reaction which involves a proton and a helium atom is one of the simpler systems which may be used to study electron transfer. As indicated in the reviews of Bayfield⁴ and Thomas⁵ this subject has received considerable experimental and theoretical attention over the past several decades. A complete description of the electron-transfer process is still lacking, however, particularly in the intermediate velocity range near 1 a.u., i.e., 25 keV for protons.

Table I lists previous studies of $H(n=3)$ atoms produced in $H^+ + He$ collisions in which the cross sections for producing individual l levels have been measured. Most of these studies observed the Balmer- α radiation as a function of position into or downstream from the collision cell and utilized the different lifetimes of the $3s$, $3p$, and $3d$ states to separate the signals from the three angular momentum levels. Major sources of error with this technique include the change in lifetimes produced by stray electric fields via Stark mixing, cascade contributions to the population of the long-lived $3s$ state, and the numerical difficulties encountered in unfolding three exponential signals from the background.

Few measurements of the cross sections for producing individual (l, m_l) sublevels have been performed. The polarization of the radiation from the $3d$ state has been measured by Hughes *et al.*⁶ but no conclusions concerning the sublevel cross sections were drawn. Preliminary measurements of the individual $n=3$, (l, m_l) sublevel cross sections at 50-keV collision energy have been made by Brower and Pipkin⁷ using the microwave resonance optical detection technique.⁸

Quantum-beat experiments which measure the orientation and alignment of excited atomic states have been discussed in the review of Berry and Hass⁹ and in references therein. In particular, several techniques have been used to measure the coherent excitation of angular momentum levels in collisionally produced hydrogen atoms. One

TABLE I. Previous measurements of electron transfer to the $3l$ states of H in $H^+ + He$ collisions.

State ($3l$)	Author	Energy range (keV)
3s	Conrads <i>et al.</i> ^a	80–700
	Dawson and Loyd ^b	1.2–8.2
	Edwards and Thomas ^c	75–350
	Ford and Thomas ^d	75–600
	Hughes <i>et al.</i> ^e	5–115
	Hughes <i>et al.</i> ^f	10–120
	Lenormand ^g	15–80
3p	Andreev <i>et al.</i> ^h	10–40
	Dawson and Loyd ⁱ	3.2–8.2
	Ford and Thomas ^d	75–300
	Hughes <i>et al.</i> ^f	10–100
	Lenormand ^g	15–80
	Risley <i>et al.</i> ^j	2–15
3d	Dawson and Loyd ⁱ	3.2–8.2
	Edwards and Thomas ^c	75–250
	Ford and Thomas ^d	75–250
	Hughes <i>et al.</i> ^f	10–100
	Lenormand ^g	15–80

^aR. J. Conrads, T. W. Nichols, J. C. Ford, and E. W. Thomas, *Phys. Rev. A* **7**, 1928 (1973).

^bH. R. Dawson and D. H. Loyd, *Phys. Rev. A* **9**, 166 (1974).

^cJ. L. Edwards and E. W. Thomas, *Phys. Rev. A* **2**, 2346 (1970).

^dJ. C. Ford and E. W. Thomas, *Phys. Rev. A* **5**, 1694 (1972).

^eR. H. Hughes, H. R. Dawson, B. M. Doughty, D. B. Kay, and C. A. Stigers, *Phys. Rev.* **146**, 53 (1966).

^fReference 6.

^gJ. Lenormand, *J. Phys. (Paris)* **37**, 699 (1976).

^hE. P. Andreev, V. A. Ankudinov, S. B. Bobashev, and V. B. Mateev, *Zh. Eksp. Teor. Fiz.* **52**, 357 (1967) [*Sov. Phys.—JETP* **25**, 232 (1967)].

ⁱH. R. Dawson and D. H. Loyd, *Phys. Rev. A* **15**, 43 (1977).

^jReference 39.

technique is the observation of quantum beats in the emitted radiation downstream from a foil or thin gas cell at the frequency corresponding to the energy splitting between the different states. This technique has been used to observe s - d coherences in $n=3$ and $n=4$ hydrogen atoms created in proton-carbon-foil collisions by Burns and Hancock,¹⁰ Denis *et al.*,¹¹ and Carmeliet *et al.*¹² and in $n=4$ hydrogen atoms formed in $H^+ + He$ and $H^+ + Ar$ collisions by Dehaes and Singer.¹³ Based on a suggestion of Eck,¹⁴ coherences between states with opposite parity have been measured by applying an electric field of fixed magnitude but directed parallel or antiparallel to the beam direction. This technique has been used to observe s - p coherences in $n=2$ hydrogen atoms created in proton-carbon-foil collisions by Sellin *et al.*,¹⁵ Gaupp *et al.*,¹⁶ and Gabrielse¹⁷ and in $n=2$ hydrogen

atoms created in $H^+ + He$, $H^+ + Ar$, and $H^+ + O_2$ collisions by Sellin *et al.*¹⁸ A major source of error associated with these techniques, particularly in the thin-gas-cell measurements, is the relative positioning of the target and detector. A third technique for observing coherently excited hydrogen atoms is to measure the optical signals emitted from within a collision cell as a function of electric fields applied within the cell. This technique has been used to observe coherences in $n=3$ hydrogen atoms produced in $Na^+ + H_2$ collisions by Lombardi and Giroud,¹⁹ in $e^- + H$ collisions by Mahan and Smith²⁰ and Krotkov,²¹ and in $n=2$ hydrogen atoms produced in $H + He$, $H + O_2$, and $H + N_2$ collisions by Krotkov and Stone.²² This third technique is the one used in the measurements described below.

Several different interpretations or parametrizations of the density matrix have been given in order to more fully understand the physical meaning of the density matrix. Fano and Macek²³ constructed the orientation vector and alignment tensor using combinations of angular momentum operators to describe the excited atomic state. This approach is not applicable to the $H(n=3)$ case considered here since it does not include terms to describe the coherent production of different angular momentum levels. Gabrielse and Band²⁴ gave a complete parametrization of hydrogenic density matrices in terms of electric and magnetic multipole moment operators and their time derivatives. This parametrization^{17,25,26} is unsatisfactory since the expectation values of the time derivative operators depend on the small relativistic and quantum electro-dynamical energy splittings and vanish in the limit of a degenerate hydrogen atom. Gabrielse²⁶ considered combinations of standard spherical tensors which are Hermitian, thereby producing a set of observables which completely parametrizes the hydrogen density matrix. These operators have well-defined time reversal and parity symmetries indicating that familiar operators, e.g., r , p , and L , may be used for the parametrization. Burgdörfer²⁷ has exhibited such a parametrization for any n -shell hydrogen density matrix using operators constructed from the Runge-Lenz vector A and the angular momentum L and has given an explicit parametrization of the $n=2$ and $n=3$ density matrices. Burgdörfer and Dubé²⁸ have used this parametrization to interpret the results of their calculations of the density matrix describing $H(n=3)$ atoms formed in $H^+ + He$ collisions. This interpretation is unsatisfactory since it relies on a classical orbit to provide meaning for A . Recently, this laboratory has proposed³ an interpretation based on the electron probability distribution and the electron current distribution. This interpretation is more appropriate for the case of hydrogen density matrices than previous interpretations since it is valid in the degenerate atom limit and does not rely on a classical analogy. The density matrices presented in this paper are discussed using this interpretation.

The remainder of this paper is arranged as follows. Section II describes the experimental apparatus and procedure. Section III presents the theoretical analysis of the experimental signals. Section IV presents an example of the experimental results. Section V discusses the results in terms of a physical interpretation of the density matrix.

II. EXPERIMENTAL APPARATUS AND PROCEDURE

A. General description

A (40–80)-keV proton beam passed through a collision cell filled with He gas producing hydrogen atoms in various excited states by electron-transfer collisions. Hydrogen atoms in the $n=3$ level were studied by observing the Balmer- α radiation emitted from a relatively wide viewing region at a fixed position in the collision cell. The optical detection system completely characterized the emitted radiation by measuring the four Stokes parameters.^{29,30} Uniform electric fields were applied inside the collision cell in order to produce Stark mixing of the atomic states. Two configurations of electric fields were used. Axial fields were directed parallel and antiparallel to the proton beam, and transverse fields were directed perpendicular to the proton beam. By changing the magnitude and direction of the applied electric fields, large variations in the measured Stokes parameters were induced. Analysis of these variations determined the density matrix describing the $n=3$ hydrogen atoms formed in the collision.

B. Apparatus

1. Proton beam

Figure 1 shows the (20–200)-kV Cockcroft-Walton accelerator and beam line used in this experiment. The protons were formed in a duoplasmatron ion source, extracted, focused with an einzel lens, and accelerated to the final energy. Measurements were made with proton energies of 40, 60, and 80 keV which are accurate to 1%.

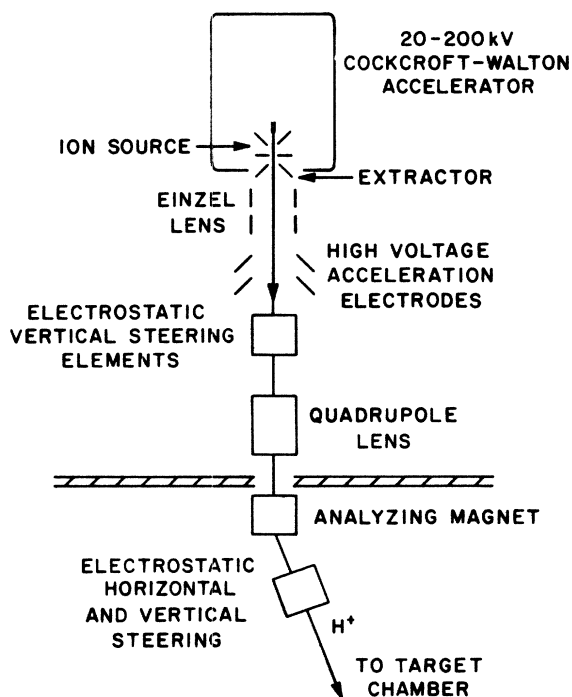


FIG. 1. Apparatus used to produce the proton beam.

After focusing with a quadrupole lens, the protons were separated from H_2^+ and H_3^+ ions by a bending magnet.

Figure 2 shows the relative positioning of the collision cell, optical system, and Faraday cup. The proton beam was collimated by two 1.6-mm-diam apertures located 26 cm apart before entering the collision cell through a 3-mm-diam aperture. After passing through the cell, the protons were collected in a Faraday cup biased at +90 V to prevent the loss of secondary electrons. Because the collection efficiency of the Faraday cup was found to vary by as much as 5% depending on the magnitude and direction of the axial electric fields applied in the collision cell, axial field data were normalized to a preset amount of time. No dependence of the Faraday-cup collection efficiency was found to within 1% when the transverse electric fields were applied; therefore, transverse field data were normalized to a preset amount of beam. The ion beam current was stable to within 1%. Typical beam currents were 0.5–1.0 μA .

2. Collision cell and electric fields

The collision cell was filled with He gas at a pressure 0.5–1.0 mTorr as measured with a capacitance manometer. When the collision cell was filled with He, the pressure in the beam line outside the entrance aperture in Fig. 2 was at least a factor of 100 below the pressure in the collision cell.

All parts located near the collision cell were made of nonmagnetic materials. A double-layer mu-metal shield surrounded the collision cell and reduced the earth's magnetic field to less than 5 mG. The resulting motional electric field for an 80-keV hydrogen atom was less than 0.02 V/cm.

Figure 3 shows the collision-cell configuration when axial electric fields were applied. Equal positive and nega-

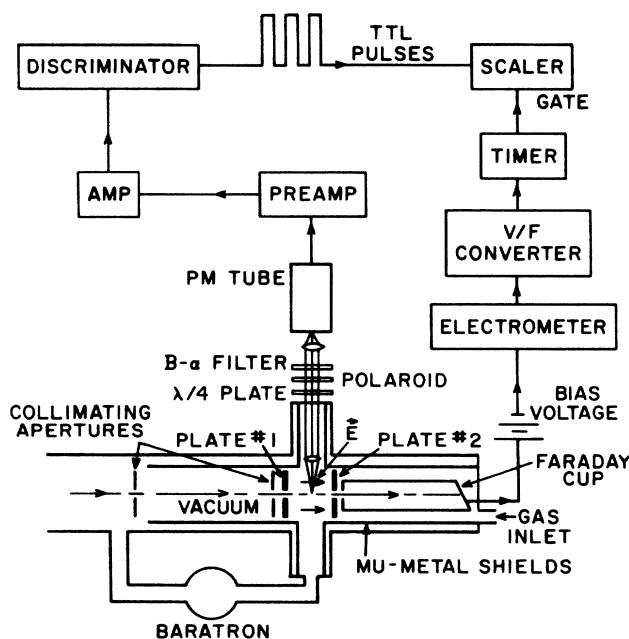


FIG. 2. Collision cell and the data-acquisition components.

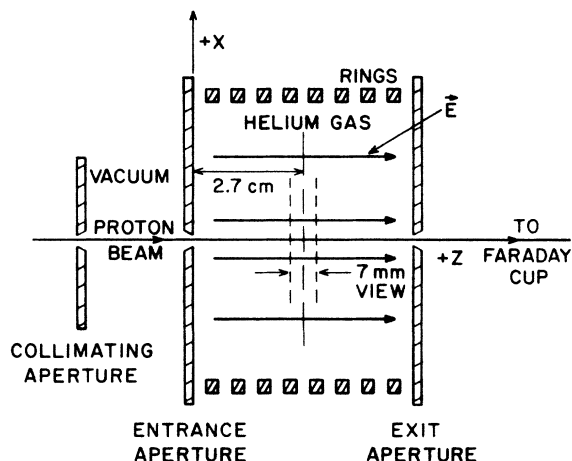


FIG. 3. Collision-cell configuration for axial electric fields.

tive voltages were applied to the entrance and exit aperture walls of the collision cell to produce electric fields in the range -600 to $+600$ V/cm with an accuracy of 0.3%. Voltages were applied to the intermediate rings to produce more uniform electric fields. No corrections were made for the small nonuniformities of the fields caused by the entrance aperture, exit aperture, and ring spacing and size. Positive fields were defined as those fields oriented in the direction of the proton beam.

Figure 4 shows the collision-cell configuration for transverse electric fields. The entrance aperture was grounded and equal positive and negative voltages were applied to produce electric fields which were directed perpendicularly to the proton beam axis and observation direction. The pair of plates to the right of the entrance aperture helped ensure the uniformity of the electric field close to the entrance aperture. The direction of positive electric fields is indicated in Fig. 5. The applied electric fields were in the range -800 to $+800$ V/cm with an ac-

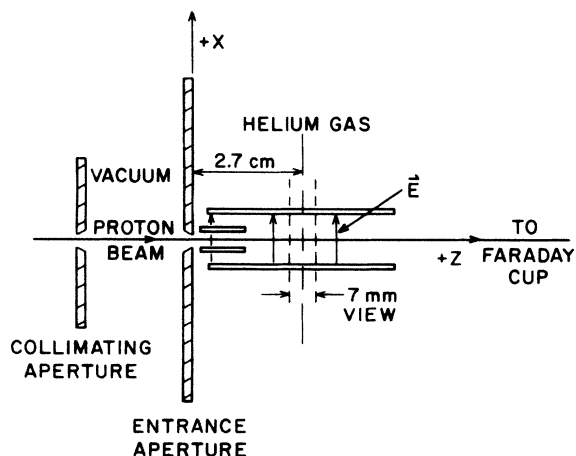


FIG. 4. Collision-cell configuration for transverse electric fields. The fields are directed perpendicular to the proton beam axis and observation direction.

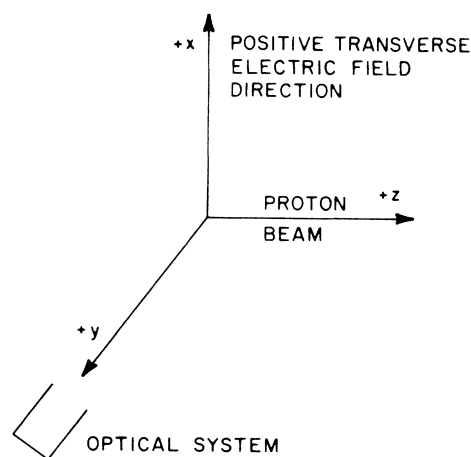
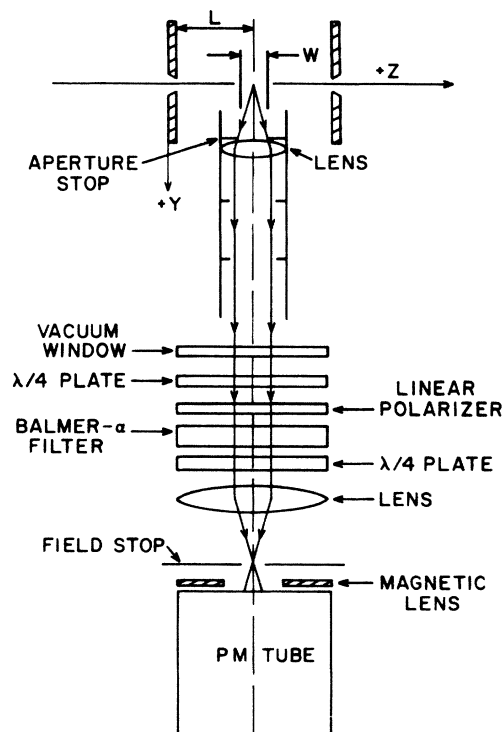


FIG. 5. Coordinate system indicating the direction of positive transverse electric fields.

curacy of 1%. No corrections were made for the nonuniformities in the electric fields whose sources included the grounded entrance aperture and the finite size of the plates between which the potential difference was applied.

3. Optical system

An EMI 9658A photomultiplier tube with a Balmer- α filter and appropriate polarizers detected the emitted radiation. The $f/6.35$ optical system viewed a 0.700 ± 0.025 -cm length of beam centered 2.70 ± 0.08 cm into the gas cell. As shown in Fig. 6, the system included an

FIG. 6. Optical system. The linear polarizer and the $\lambda/4$ plate closest to the collision region were included only for those measurements in which they were needed (see text).

aperture stop, a field stop, two lenses, and an interference filter with a bandpass of 11 nm centered at 656 nm. A linear polarizer and $\lambda/4$ plate were included for the polarization measurements. A second $\lambda/4$ plate produced circularly polarized radiation to reduce the polarization sensitivity of the photomultiplier tube which was caused by its prismatic window. The prismatic window was oriented at 45° to the beam direction.

The emitted radiation is completely characterized by the Stokes parameters^{29,30} which are defined as follows:

$$\begin{aligned} S_0 &= I_{\parallel} + I_{\perp} , \\ S_1 &= I_{\parallel} - I_{\perp} , \\ S_2 &= I_{45^\circ} - I_{135^\circ} , \end{aligned} \quad (1)$$

and

$$S_3 = I_{RH} - I_{LH} ,$$

where I_{\parallel} , I_{\perp} , I_{45° , and I_{135° are intensities passing through an ideal linear polarizer oriented at angles of 0° , 90° , 45° , and 135° with respect to the proton beam, respectively; and I_{RH} and I_{LH} are the intensities of right- and left-handed circularly polarized radiation, respectively. For light emitted in the $+y$ direction, the polarization vectors corresponding to the intensities needed to evaluate the Stokes parameters are listed in Table II. The apparatus, data collection, and experimental results will be presented in terms of the Stokes parameters since these quantities provide a more standard method of characterizing the emitted radiation than the total intensity, the intensity at 45° , and the linear and circular polarization fractions which were used in Refs. 1–3. When S_0 was measured, the linear polarizer was removed. When S_3

TABLE II. Cartesian components of the polarization vectors ϵ used to evaluate the intensities of radiation emitted in the $+y$ direction. When combined with the factor $e^{i(ky - \omega t)}$ the polarization vectors for the circularly polarized radiation give radiation polarized in the optical sense, i.e., a snapshot of the tip of the electric field vector forms a right- or left-handed helix along the $+y$ propagation axis.

Intensity	ϵ ($\epsilon_x, \epsilon_y, \epsilon_z$)
I_{\parallel}	(0, 0, 1)
I_{\perp}	(1, 0, 0)
I_{45°	$\left[\frac{1}{\sqrt{2}}, 0, \frac{1}{\sqrt{2}} \right]$
I_{135°	$\left[\frac{1}{\sqrt{2}}, 0, -\frac{1}{\sqrt{2}} \right]$
I_{RH}	$\left[\frac{1}{\sqrt{2}}, 0, \frac{i}{\sqrt{2}} \right]$
I_{LH}	$\left[\frac{1}{\sqrt{2}}, 0, -\frac{i}{\sqrt{2}} \right]$

was measured, the $\lambda/4$ plate closest to the viewing region was included.

C. Procedure

1. Data collection

When axial electric fields were applied, the reflection symmetry through a plane containing the axes of the proton beam and the optical system allowed only S_0 and S_1 to be nonzero. When transverse fields were applied, the reflection symmetry was broken and all four Stokes parameters were allowed to be nonzero. Thus, six sets of optical signals versus electric field were measured for each collision energy studied.

With the transverse electric field arrangement, S_0 and S_1 were required to be symmetric and S_2 and S_3 were required to be antisymmetric for positive and negative electric fields because a reflection through the plane containing the axes of the proton beam and the optical system was equivalent to the application of a negative electric field. To check for systematic errors, the experimental signals were measured for both polarities of electric field, except for the signals needed to determine S_2 . No similar reflection symmetry existed for the axial electric field arrangement and the experimental signals were measured for both positive and negative electric fields.

When axial electric fields were applied, data were collected for both positive and negative electric fields as follows: from 0 to 55.6 V/cm in 9.3 V/cm steps, from 55.6 to 148.2 V/cm in 18.5 V/cm steps, and from 148.2 to 555.9 V/cm in 37.1 V/cm steps. These measurements gave a total of 45 data points for each of the two Stokes parameters measured. When transverse electric fields were applied, data were collected for both positive and negative electric fields as follows: from 0 to 44.1 V/cm in 3.2 V/cm steps, from 0 to 189 V/cm in 7.9 V/cm steps, from 189 to 378 V/cm in 15.8 V/cm steps, and from 378 to 725 V/cm in 31.5 V/cm steps. These measurements gave a total of 119 data points for each of the four Stokes parameters measured. Thus a total of 566 data points were measured for each collision energy studied.

Typical counting rates were on the order of 500 counts/s. At least 10000 counts were collected for each datum point. For the transverse field measurements, the counting period was defined by the time to collect a preset amount of charge in the Faraday cup. For the axial field measurements, the counting period was taken to be a predetermined time interval since the collection efficiency of the Faraday cup depended on the applied axial fields. This procedure introduced an additional random error due to the short time variations of the proton beam current which were approximately 1%.

Background counting rates were on the order of 60 counts/s. For each experimental configuration, the background was measured by removing the He gas and counting for the same period which was used to determine the signal. Background rates were measured as a function of electric field and showed similar but much smaller variations as the signals measured with the He target gas.

Since the absolute detection efficiency of the optical

system was not measured, the Stokes parameters as defined by the intensities in Eqs. (1) were normalized by setting S_0 to unity at zero electric field,

$$S_0(E=0)=1. \quad (2)$$

The first Stokes parameter $S_0(E)$ was determined by alternately measuring the total intensity signal with zero electric field $I_T(E=0)$ and with an electric field of desired value $I_T(E)$,

$$S_0(E)=\frac{I_T(E)-B_T(E)}{[I_T(E=0)]_{av}-B_T(E=0)}, \quad (3)$$

where $B_T(E)$ is the background signal and $[I_T(E=0)]_{av}$ is the average of the $I_T(E=0)$ signals which had been collected immediately before and after $I_T(E)$. This procedure normalized the measurements according to Eq. (2) and helped to account for slow drifts in the gas pressure and proton beam current.

The second Stokes parameter $S_1(E)$ was determined by measuring the linear polarization fraction and multiplying by the total intensity $S_0(E)$,

$$S_1(E)=S_0(E)\frac{[I_{||}(E)-B_{||}(E)]-[I_{\perp}(E)-B_{\perp}(E)]}{[I_{||}(E)-B_{||}(E)]+[I_{\perp}(E)-B_{\perp}(E)]}, \quad (4)$$

where $I_{||}(E)$ and $I_{\perp}(E)$ are the signals measured with the linear polarizer oriented parallel and perpendicular to the proton beam axis, respectively.

The third Stokes parameter $S_2(E)$ was measured by orienting the linear polarizer at an angle of 45° with respect to the proton beam and alternately measuring the signal with zero electric field $I_{45^\circ}(E=0)$ and with an electric field of the desired value $I_{45^\circ}(E)$. $S_2(E)$ was found by normalizing the signals to the average of the $E=0$ signals as in Eq. (3) and using the fact that $I_{135^\circ}(E)$ and $I_{45^\circ}(-E)$ were equivalent,

$$S_2(E)=\frac{1}{2}\left[\frac{I_{45^\circ}(E)-B_{45^\circ}(E)}{[I_{45^\circ}(E=0)]_{av}-B_{45^\circ}(E=0)}-\frac{I_{45^\circ}(-E)-B_{45^\circ}(-E)}{[I_{45^\circ}(E=0)]_{av}-B_{45^\circ}(E=0)}\right], \quad (5)$$

where the factor of $\frac{1}{2}$ enters because, with the normalization expressed in Eq. (2), $I_{45^\circ}(E=0)=0.5$. In retrospect, this procedure for measuring $S_2(E)$ was less than ideal since it forced $S_2(E)$ to be antisymmetric in E . Separate measurements of $I_{45^\circ}(E)$ and $I_{135^\circ}(E)$ should have been made in order to provide an experimental check of the antisymmetry of $S_2(E)$.

The fourth Stokes parameter $S_3(E)$ was obtained by measuring the circular polarization fraction and multiplying by $S_0(E)$,

$$S_3(E)=S_0(E)\frac{[I_{RH}(E)-B_{RH}(E)]-[I_{LH}(E)-B_{LH}(E)]}{[I_{RH}(E)-B_{RH}(E)]+[I_{LH}(E)-B_{LH}(E)]}. \quad (6)$$

As discussed above, $S_3(E)$ should be completely antisymmetric for positive and negative electric fields. The measured differences contained a symmetric part which could be accounted for if the retardation angle of the $\lambda/4$ plate

deviated from 90° by 7° . The antisymmetrized Stokes parameter $S_3^A(E)$ was formed by removing the symmetric component of the signal,

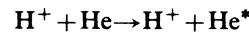
$$S_3^A(E)=\frac{S_3(E)-S_3(-E)}{2}. \quad (7)$$

2. Systematic checks

The optical signals are expected to be proportional to the proton beam current and target gas density. The signals were demonstrated to be linear with these variables to within the 1% statistical counting accuracy of the measurements.

It was verified that the optical system correctly identified the sense of the polarized radiation by (i) observing a linearly polarized reflection from a surface and (ii) observing the circularly polarized radiation of known handedness produced with a Mooney rhomb.³¹

In order to measure the residual polarization of the detector system, unpolarized radiation from the He 3^1S-2^1P transition produced in the collision



was observed by removing the Balmer- α filter and replacing it with a filter which passed the 728-nm radiation. The polarization fraction of the optical system was measured to be -0.01 ± 0.01 and was used to correct the Balmer- α signals.

The 728-nm line of He was also used to test for possible variations of the intensity or polarization signals induced by the applied electric fields. For the total intensity measurement with axial electric fields, a systematic error of approximately the same size as the 1% statistical counting errors was observed. Within the statistical counting errors, no systematic errors were observed for other electric field and optical system configurations.

III. DETERMINATION OF THE DENSITY MATRIX

In order to analyze the experimentally observed Balmer- α signals, a theoretical description of the hydrogen atoms formed in the collision is needed. Atoms formed at a particular impact parameter may be described by a pure state consisting of a linear superposition of hydrogenic states. The Balmer- α signals were produced by atoms created in collisions at different impact parameters. These atoms are described by incoherently summing the pure states produced at each impact parameter. The resulting mixed state is conveniently described by the density matrix.

As discussed below, the density matrix for the collisionally produced $H(n=3)$ atoms is completely determined by 14 independent quantities. The density matrix was determined by expressing it as a superposition of 14 basis matrices. The coefficients used in the superposition were evaluated by numerically calculating the six Balmer- α optical signals (Stokes parameters) that would have been produced by each basis matrix and numerically fitting these theoretical signals to the experimental observations.

A. Density-matrix description of the collisionally produced hydrogen atoms

The hydrogen atoms were described in the nlm_l representation since the collision time ($\sim 10^{-16}$ s) was much shorter than the spin-orbit period ($\sim 10^{-9}$ s). A representation in terms of Stark states could also have been used initially, but because fine structure and the Lamb shift must be incorporated into the analysis of the time dependence, the nlm_l representation was a better choice. A collision at impact parameter \mathbf{b} creates a hydrogen atom in a pure state described by the wave function $\Psi(\mathbf{b})$ which may be expressed as a superposition of hydrogen eigenfunctions ψ_{nlm_l} ,

$$\Psi(\mathbf{b}) = \sum_{n,l,m_l} a_{nlm_l}(\mathbf{b}) \psi_{nlm_l}. \quad (8)$$

The 9×9 density matrix which describes the $H(n=3)$ atoms has elements which are given by

$$\rho_{lm_l, l'm_l'}^L = \int_0^{2\pi} \int_0^\infty a_{3lm_l}(\mathbf{b}) a_{3l'm_l'}^*(\mathbf{b}) b db d\phi. \quad (9)$$

The normalization of ρ^L is such that $\text{Tr}(\rho^L)$ is equal to the total cross section for electron transfer into the $n=3$ manifold.

Restrictions on the values of the density-matrix elements result from symmetries in the collision.³² Cylindrical symmetry allows only elements between states of the same m_l to be nonzero,

$$\rho_{lm_l, l'm_l'}^L = \rho_{lm_l, l'm_l'}^L \delta_{m_l m_l'}. \quad (10)$$

Reflection and cylindrical symmetries allow the elements to depend only on $|m_l|$,

$$\rho_{lm_l, l'm_l'}^L = \rho_{l-m_l, l'-m_l'}^L. \quad (11)$$

Also, the density matrix is Hermitian,

$$\rho_{lm_l, l'm_l'}^L = (\rho_{l'm_l', lm_l}^L)^*. \quad (12)$$

These constraints allow only 14 independent quantities to completely determine the $n=3$ ρ^L , six (real) diagonal elements and the real and imaginary parts of four off-diagonal elements. The density matrix is shown in Fig. 7.

The magnitude of the diagonal and off-diagonal density-matrix elements are limited,

$$\rho_{lm_l, lm_l}^L \geq 0 \quad (13)$$

and

$$|\rho_{lm_l, l'm_l'}^L| \leq (\rho_{lm_l, lm_l}^L \rho_{l'm_l', l'm_l'}^L)^{1/2}. \quad (14)$$

The diagonal elements of the density matrix are proportional to the cross sections for forming particular lm_l states. The off-diagonal elements give the coherence or average phase difference between states induced by the collision.

B. Optical signals produced by a density matrix

The Balmer- α signals calculated from a specific density matrix must take into account the time evolution from the

	s_0	p_{+1}	p_0	p_{-1}	d_{+2}	d_{+1}	d_0	d_{-1}	d_{-2}
s_0	$\rho_{s_0 s_0}$		$\rho_{s_0 p_0}$				$\rho_{s_0 d_0}$		
p_{+1}		$\rho_{p_{+1} p_{+1}}$				$\rho_{p_{+1} d_{+1}}$			
p_0	$\rho_{s_0 p_0}^*$		$\rho_{p_0 p_0}$				$\rho_{p_0 d_0}$		
p_{-1}				$\rho_{p_{-1} p_{-1}}$				$\rho_{p_{-1} d_{-1}}$	
d_{+2}					$\rho_{d_{+2} d_{+2}}$				
d_{+1}		$\rho_{p_{+1} d_{+1}}^*$				$\rho_{d_{+1} d_{+1}}$			
d_0	$\rho_{s_0 d_0}^*$		$\rho_{p_0 d_0}^*$				$\rho_{d_0 d_0}$		
d_{-1}				$\rho_{p_{-1} d_{-1}}^*$				$\rho_{d_{-1} d_{-1}}$	
d_{-2}									$\rho_{d_{-2} d_{-2}}$

FIG. 7. $H(n=3)$ density matrix. The elements depend only on $|m_l|$, e.g., $\rho_{p_{+1} p_{+1}} = \rho_{p_{-1} p_{-1}}$. Elements which are not shown are equal to zero.

collision to the point of observation, the integration over all points of excitation and decay, the polarization of the emitted radiation, and the emission direction with respect to the ion beam and applied electric field.

1. Time evolution

The time evolution of the density matrix is governed by the Hamiltonian. In order to include the relativistic and quantum electrodynamical energy splittings, the electron spin was included by transforming the initial density matrix ρ^L to an 18×18 density matrix ρ^J . This transformation was carried out by constructing an 18×18 density matrix ρ^{LS} in the $lm_l sm_s$ representation with elements

$$\rho_{lm_l sm_s, l'm_l' sm_s'}^L = \rho_{lm_l, l'm_l'}^L \rho_{sm_s, sm_s'}^S, \quad (15)$$

where ρ^S is a 2×2 spin density matrix in the (s, m_s) representation. Since the spin was assumed to be unaffected by the collision, the $t=0$ elements of ρ^S are given by

$$\rho_{sm_s, sm_s'}^S(t=0) = \frac{1}{2} \delta_{m_s m_s'}. \quad (16)$$

Transforming to the (l, s, j, m_j) representation gives ρ^J ,

$$\rho^J = U^\dagger \rho^{LS} U, \quad (17)$$

where U is the transformation matrix of Clebsch-Gordan coefficients between the (l, m_l, s, m_s) and the (l, s, j, m_j) representations. The matrix U has elements $\langle lm_l sm_s | lsjm_j \rangle$.

The time evolution of the density matrix is given by

$$\rho(t) = e^{-iHt/\hbar} \rho(t=0) e^{+iHt/\hbar}, \quad (18)$$

where the complex Hamiltonian H may be written as

$$H = H_0 + e\mathbf{r} \cdot \mathbf{E} - i\hbar\Gamma/2, \quad (19)$$

where H_0 is the unperturbed, time-independent Hamiltonian which includes the relativistic and quantum electrodynamical energy splittings; $e\mathbf{r}\cdot\mathbf{E}$ gives the Stark interaction; and $i\hbar\Gamma/2$, where Γ is the transition rate to all lower states, is included to describe the decay phenomenologically.

The Bethe-Lamb approximation, which is used to account for the decay phenomenologically in Eq. (19), is expected^{33,34} to be valid for the $n=3$ shell of hydrogen because of the near degeneracy of the lm_l sublevels within the $n=3$ shell compared to the large energy difference between the $n=3$ and $n=1,2,4,5,\dots$ shells which would be mixed in by the applied electric field. Within the $n=3$ manifold, the approximation is expected to be valid²⁵ since states with the same rotational symmetry are widely spaced compared to their widths. The validity of the approximation has been studied by making quantum electrodynamical calculations of the decay from hydrogen atoms in the $n=2$ state.³⁵⁻³⁸ In particular, Lévy³⁸ finds the approximation to be valid to the order of α^2 .

Hyperfine interactions were not included in the Hamiltonian H . Hyperfine structure causes the nuclear spins to become polarized so that the emitted radiation exhibits less polarization and a more isotropic angular distribution. These effects could be observable for the $n=3$ level since the hyperfine splittings, which are listed in Table III, are comparable to the $n=3$ decay rates. In order to evaluate the effect of hyperfine structure, sample calculations which included the hyperfine splittings were carried out for both high and low (zero) electric fields. These calculations indicated that the neglect of hyperfine structure causes less than a 1% error in the calculated optical signals. Because this error is smaller than errors from other sources [e.g., cascade (see below)], the increased cost in computer time needed for the inclusion of hyperfine structure in the Hamiltonian H was not justified and hyperfine interactions have been neglected in the calculated signals discussed in this paper.

Also neglected from the Hamiltonian was the increase in the $n=3$ population due to cascade. The $n=4$ level is the most important source of cascade because higher n levels have smaller cross sections^{4,39} and lower branching ratios to the $n=3$ level.⁴⁰ In addition, the $n > 4$ levels have longer lifetimes⁴⁰ so that fewer atoms decay while in

TABLE III. $H(n=3)$ level parameters. Energies are given with respect to the ${}^2P_{1/2}$ state. Γ is the transition rate to all final states. ΔE_{HFS} is the hyperfine splitting.

State	H_0^a (MHz)	Γ^b (MHz)	ΔE_{HFS}^c (MHz)
${}^2S_{1/2}$	314.898	6.3136	52.6
${}^2P_{1/2}$	0.0	189.70	17.5
${}^2P_{3/2}$	3250.089	189.70	7.02
${}^2D_{3/2}$	3244.757	64.651	4.21
${}^2D_{5/2}$	4328.095	64.651	2.71

^aH. J. Beyer, in *Progress in Atomic Spectroscopy*, edited by W. Hanle and H. Kleinpoppen (Plenum, New York, 1978), p. 529.

^bCalculated using Eq. (59.12) and related equations of Ref. 40.

^cCalculated using Eq. (22.12) of Ref. 40.

the field of view of the optical system. When the electric field is zero, the $4s$ - $3p$ cascade is the major source of error since other l levels within the $n=4$ manifold have lower formation cross sections⁴ and, except for the $4f$ state, smaller branching ratios to the $n=3$ state.⁴⁰ Using the $4s$ cross section measured by Hughes *et al.*,⁴¹ the cascade contribution to the $3p$ population was estimated to be 2% for a 40-keV collision energy. An estimate of the cascade contribution to the population of the $n=3$ level was also made in the case in which electric fields are applied and the $n=4$ levels are fully mixed. This estimate used an average lifetime and branching ratio to the $n=3$ level⁴⁰ and a total $n=4$ cross section derived from the total $n=3$ cross section of Hughes *et al.*⁶ and the n^{-3} scaling relation.^{4,39} The cascade contribution to the $n=3$ level was estimated to be 3%. Similar errors are assumed to hold for intermediate values of electric field and for cascade contributions to the off-diagonal density-matrix elements.

The effect of the Stark interaction on the energy levels and lifetimes of the $n=3$ state may be illustrated by constructing the Hamiltonian matrix H^J in the (l,s,j,m_j) representation with elements $\langle lsjm_j | H | l'sj'm'_j \rangle$. Matrix elements of H_0^J and Γ^J are given in Table III. As shown in Appendix A, matrix elements of the Stark term are

$$\begin{aligned} &\langle lsjm_j | e\mathbf{r}\cdot\mathbf{E} | l'sj'm'_j \rangle \\ &= (-1)^{l+s-m_j} \sqrt{(2j+1)(2j'+1)} \begin{Bmatrix} j' & 1 & j \\ l & s & l' \end{Bmatrix} \\ &\quad \times e \langle l || \mathbf{r} || l' \rangle \sum_q (-1)^q E_{-q} \begin{Bmatrix} j' & 1 & j \\ m'_j & q & -m_j \end{Bmatrix}, \quad (20) \end{aligned}$$

where the electric field is given by its spherical components [see, for example, Eq. (5.1.3) of Edmonds⁴²],

$$E_0 = E_z \quad \text{and} \quad E_{\pm 1} = \mp \frac{1}{\sqrt{2}} (E_x \pm iE_y). \quad (21)$$

The Hamiltonian matrix was diagonalized using the matrix S obtained in a numerical diagonalization routine,⁴³

$$\Lambda = S^{-1} H^J S, \quad (22)$$

where Λ is a complex diagonal matrix whose elements are the eigenvalues λ_i . The real and imaginary parts of the eigenvalues λ_i which correspond to the energy levels and widths of the $n=3$ hydrogen atom in an electric field are shown in Figs. 8 and 9. Figure 8 is similar to the results of Lüders⁴⁴ who calculated the eigenvalues for the $n=3$ manifold for a Hamiltonian similar to Eq. (19) but which did not include the Lamb-shift splitting or decay.

The exponential terms in Eq. (18) may be simplified using Eq. (22) giving

$$\rho^J(t) = S e^{-i\Lambda t/\hbar} S^{-1} \rho^J(t=0) (S^\dagger)^{-1} e^{+i\Lambda^\dagger t/\hbar} S^\dagger. \quad (23)$$

2. Populations of radiating $H(n=3)$ atoms

To determine the intensity of radiation observed by the optical system, the number of atoms within the viewing region, given by a number matrix, N_{obs}^J , must be known. The number matrix of atoms, N_{prod}^J , produced per unit time t and per unit length z in the collision cell is given by

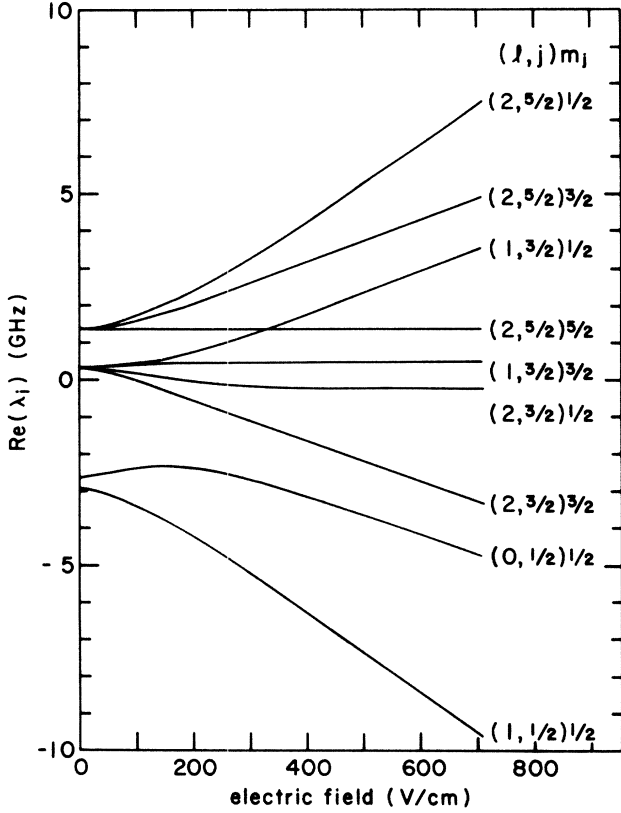


FIG. 8. Energy levels $\text{Re}(\lambda_i)$ of an $\text{H}(n=3)$ atom as a function of an applied electric field. The states are labeled as $(l, j)m_j$ where l and j refer to the state of an unperturbed hydrogen atom from which the state evolves when the electric field is adiabatically switched on and where m_j is the magnetic sublevel quantum number where the quantization axis is taken to be in the direction of the electric field. When the electric field is applied, only m_j is a good quantum number.

$$\frac{d^2 N_{\text{prod}}^J}{dt dz} = n_{\text{He}} i \rho^J(t=0), \quad (24)$$

where n_{He} is the number density of He atoms and i is the proton beam current (in units of protons/s). The matrix of atoms within the observation region depends on the distance between the point at which the collision occurred and the point of observation z_{obs} ,

$$\frac{d^2 N_{\text{obs}}^J}{dz_{\text{obs}} dz} = \frac{1}{v} n_{\text{He}} i \rho^J(t=(z_{\text{obs}}-z)/v), \quad (25)$$

where $dz_{\text{obs}} = v dt$. Integrating Eq. (25) over the points in the collision cell which produced excited atoms and over

$$\tilde{\rho}_{rs}^J = \frac{\Gamma_{\text{av}}}{z_2 - z_1} \sum_{k,l,m,n} S_{rk}(S^{-1})_{kl} \rho_{lm}^J(t=0) [(S^\dagger)^{-1}]_{mn} (S^\dagger)_{ns} \int_{z_1}^{z_2} \int_0^{z_{\text{obs}}} \frac{\exp[-i(\lambda_k - \lambda_n^*)(z_{\text{obs}} - z)/\hbar v]}{v} dz dz_{\text{obs}}. \quad (28)$$

For the case of transverse electric fields, the integrations in Eq. (28) were performed and $\tilde{\rho}^J$ could be written

$$\tilde{\rho}_{rs}^J = \frac{\Gamma_{\text{av}}}{z_2 - z_1} \sum_{k,l,m,n} S_{rk}(S^{-1})_{kl} \rho_{lm}^J(t=0) [(S^\dagger)^{-1}]_{mn} (S^\dagger)_{ns} \frac{1}{\alpha_{kn}} \left[\frac{e^{\alpha_{kn} z_1} - e^{\alpha_{kn} z_2}}{\alpha_{kn}} - (z_2 - z_1) \right], \quad (29)$$

where

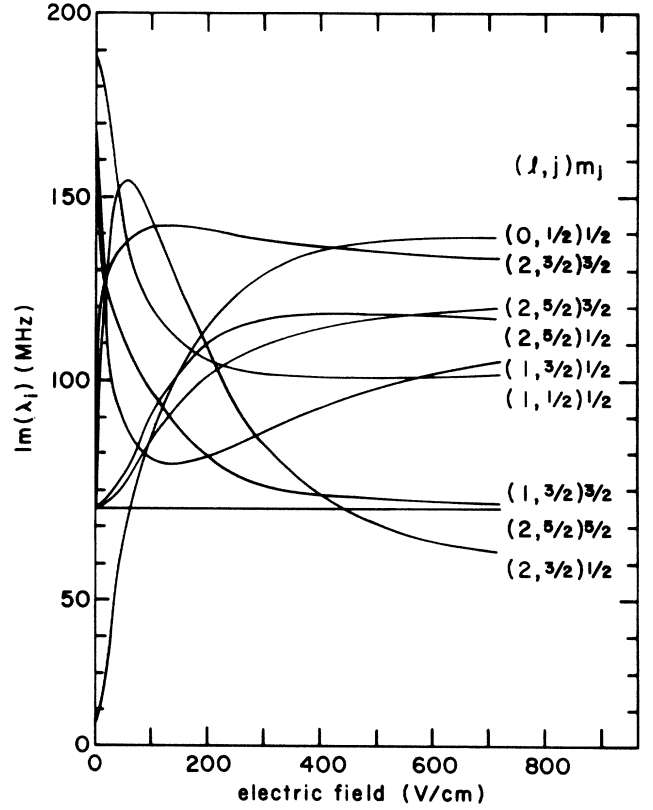


FIG. 9. Decay rates $\text{Im}(\lambda_i)$ of an $\text{H}(n=3)$ atom as a function of an applied electric field. The states are labeled as $(l, j)m_j$ (see caption for Fig. 8).

the points in the viewing region gives

$$N_{\text{obs}}^J = n_{\text{He}} i \frac{z_2 - z_1}{\Gamma_{\text{av}}} \tilde{\rho}^J, \quad (26)$$

where the viewing region extends from z_1 to z_2 (see Fig. 10), $\Gamma_{\text{av}} = 99.852$ MHz is the average decay rate for the $n=3$ manifold,⁴⁰ and the integrated density matrix $\tilde{\rho}$ is given by

$$\tilde{\rho}^J = \frac{\Gamma_{\text{av}}}{z_2 - z_1} \int_{z_1}^{z_2} \int_0^{z_{\text{obs}}} \frac{1}{v} \rho^J((z_{\text{obs}} - z)/v) dz dz_{\text{obs}}. \quad (27)$$

The factor $\Gamma_{\text{av}}/(z_2 - z_1)$ is included in Eqs. (26) and (27) so that the dimensions of $\tilde{\rho}$ and ρ are the same.

Since it was desired to perform the integrations in Eq. (27) analytically, $\rho^J(t)$ was expressed as a sum of matrix elements which allowed the time-dependent factors in Eq. (23) to be written explicitly,

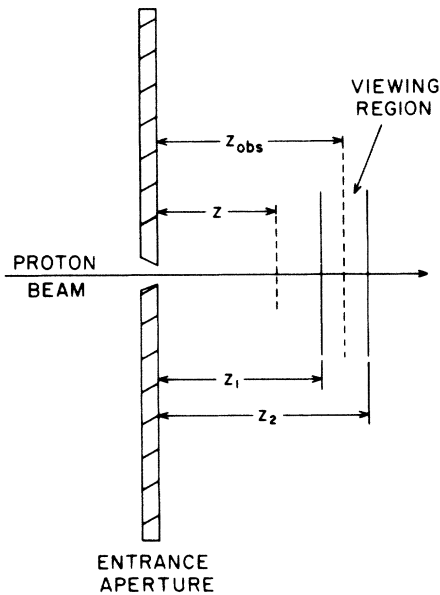


FIG. 10. Coordinates used for the integration over the collision and viewing regions.

$$\alpha_{kn} = \frac{-i(\lambda_k - \lambda_n^*)}{\hbar v} \quad (30)$$

When axial fields were applied, the protons were accelerated or decelerated inside the cell before undergoing the collisions. This change in velocity can affect the observed signals two ways. First, the factors of the velocity v in Eq. (28) introduce a kinematic effect which was taken into account in the analysis (see below). Second, the change in collision energy causes variations in the density matrix $\rho^J(t=0)$ in Eq. (28) which were not included in the analysis.

In accounting for the kinematic effects, it is noted that when the protons are accelerated, more hydrogen atoms

reach the viewing region since they have less of a chance to decay. On the other hand, the hydrogen atoms pass through the viewing region faster and are observed for a shorter period of time. In order to take this change of velocity into account, the velocity v in Eq. (28) was expressed as a function of position. Specifically, the collision cell was divided into slices and the velocity of the atoms created in each slice was taken as the proton velocity at the center of the slice. The integrations specified in Eq. (28) were carried out analytically for each slice and the results summed. The result of this investigation showed that the change in the factors of v in Eq. (28) gave less than a 0.5% change in the calculated signals for the maximum electric field used in the experiment.

The energy dependence of the density matrix $\rho^J(t=0)$ was not taken into account in the analysis because it is not known how each matrix element changes with energy. However, to estimate the size of the error introduced by the variations of $\rho^J(t=0)$, the energy dependence of the cross sections as measured by Hughes *et al.*⁶ was used. The results of this analysis indicated that the experimental signals would exhibit less than a 2% asymmetry for the maximum value of axial electric fields used.

The integrated density matrix $\tilde{\rho}^J$ was reduced to $\tilde{\rho}^L$ in the lm_l representation by inverting the transformation in Eq. (17) and taking the trace over the spin,

$$\tilde{\rho}_{lm_l, l'm'_l}^L = \sum_{m_s} \tilde{\rho}_{lm_l m_s, l'm'_l m_s}^J \quad (31)$$

3. Optical signals

The calculated optical signals were found by determining the intensity of radiation I (in units of photons/s) of polarization ϵ emitted into a solid angle $\Delta\Omega$. This rate was found by averaging over the initial states lm_l and $l'm'_l$ of the $n=3$ level, weighted by their populations, and summing over the final states $l_f m_{l_f}$ of the $n=2$ level,

$$I(\epsilon) = \frac{e^2 \omega^3}{2\pi \hbar c^3} n_{\text{He}} i \Delta\Omega \frac{z_2 - z_1}{\Gamma_{\text{av}}} \sum_{\substack{l, m_l, l', m'_l, \\ l_f, m_{l_f}}} \langle l_f m_{l_f} | \epsilon^* \cdot \mathbf{r} | lm_l \rangle \tilde{\rho}_{lm_l, l'm'_l}^L \langle l'm'_l | \mathbf{r} \cdot \epsilon | l_f m_{l_f} \rangle \quad (32)$$

As indicated in Fig. 5, theoretical expressions for the optical signals emitted in the $+y$ direction were needed. The polarization vectors ϵ corresponding to each intensity needed to evaluate the Stokes parameters are listed in Table II.

Several different methods could have been used to obtain expressions for the theoretical signals from Eq. (32). Since the hydrogen wave functions are known analytically and the angular dependencies of the Stokes parameters were not needed, term-by-term evaluation of Eq. (32) could have been performed. Alternatively, Eq. (32) can be separated into geometrical and dynamical factors as described by Blum.³² The equivalent procedure used for this work is based on the technique of Nienhuis⁴⁵ extended to the case of $l \neq l'$. This procedure expresses Eq. (32) as

$$I(\epsilon) = n_{\text{He}} i \Delta\Omega \frac{z_2 - z_1}{\Gamma_{\text{av}}} \epsilon^* \cdot \vec{C} \cdot \epsilon \quad (33)$$

where the Cartesian tensor \vec{C} gives the intensity and polarization of the radiation emitted in any direction. An explicit expression for \vec{C} is derived in Appendix B.

C. Fitting procedure

The density-matrix elements were determined by fitting sets of numerically calculated optical signals (basis signals) to the experimental observations. The basis signals were found by the procedure outlined above for 14 basis matrices, corresponding to each independent element of the density matrix. For example, the basis matrix corresponding to $\rho_{p_{\pm 1}}$ had two entries, $\rho_{p_{+1}} = 1$ and $\rho_{p_{-1}} = 1$.

Similarly, the basis matrix corresponding to $\text{Im}(\rho_{p_{\pm 1}d_{\pm 1}})$ had four entries, $\rho_{p_{+1}d_{+1}}=i$, $\rho_{p_{-1}d_{-1}}=i$, $\rho_{d_{+1}p_{+1}}=-i$, and $\rho_{d_{-1}p_{-1}}=-i$. The basis signals thus consisted of the six Stokes parameters versus applied electric field, S_0 and S_1 for axial electric fields and S_0 , S_1 , S_2 , and S_3 for transverse electric fields, for each of the 14 independent elements of the density matrix ρ^L . A total of 84 independent basis signals versus electric field were generated for each of the three collision energies studied. Careful examination of the basis signals indicated that each of the 14 density-matrix elements produced distinctly different signals implying that each element can, in principle, be determined using this technique.

The basis signals were numerically calculated on the Triangle Universities Computing Center's IBM 3081 computer using a program written in double-precision FORTRAN. Using an optimizing compiler, the program required 1.5 megabytes (1 megabyte $\equiv 10^6 \times 8$ binary digits) of memory and took 2 s of CPU (central-processing-unit) time to calculate the six Stokes parameters from a given initial density matrix for each one of the 164 values of the electric field.

The accuracy of the numerical calculations of the basis signals was tested by comparing the calculated Stokes parameters for a sample density matrix with those calculated with a program developed independently by Tolk and Tully.⁴⁶ Since the calculations of Ref. 46 did not include contributions from the off-diagonal $\rho_{s_0 d_0}$ terms, these contributions were subtracted to give a direct comparison. The two calculations agreed to within 0.5% with occasional disagreements on the order of 1%. These differences are believed to be due to the different values used for the energy levels, lifetimes, and branching ratios of the

unperturbed hydrogen atom.

A linear least-squares-fitting procedure was used.⁴⁷ The procedure was unconstrained so that it was possible to evaluate density-matrix elements outside the limits expressed by Eqs. (13) and (14), i.e., negative cross sections and unbounded off-diagonal elements. Thus one test of the basis signals and fitting procedure is whether or not the fitted elements were physically meaningful.

The procedure expressed the experimentally observed Stokes parameters as a column matrix b with elements b_i . The index i corresponds to each observation, i.e., each of the measured Stokes parameters at each value of electric field. The maximum value of i was 566. The basis signals calculated from each of the 14 basis matrices were expressed as a matrix A with elements A_{ij} , where the index j ranges from 1 to 14 and the index i corresponds to each experimental observation. Fitting functions \tilde{b}_i were expressed as a superposition of the basis signals A_{ij} ,

$$\tilde{b}_i = \sum_{j=1}^{14} A_{ij} x_j, \quad (34)$$

where x_j is the fitting coefficient of the j th basis signal. These coefficients were determined by minimizing the sum of the squared residuals between the fitting function \tilde{b}_i and the observed signals b_i . This minimization gives⁴⁸ (in matrix form)

$$x = (A^T W A)^{-1} A^T W b, \quad (35)$$

where W is a diagonal matrix whose elements are the weights given to the individual measurements. For the present results, equal weights were given to each observation and W was taken to be the unit matrix.

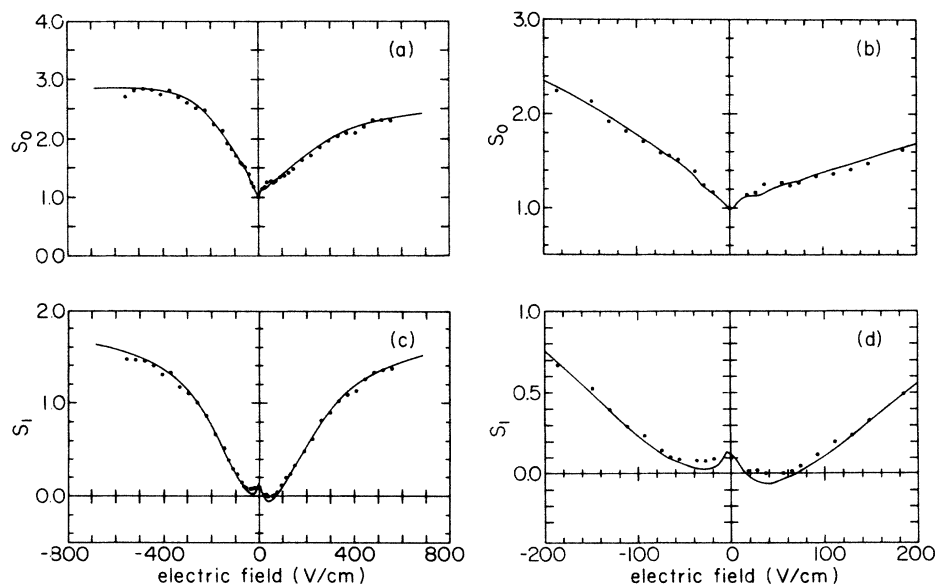


FIG. 11. Experimentally observed signals (data points) and fits (solid lines) to the signals for 60-keV $H^+ + He$ collision energy for axial electric fields. The 40- and 80-keV data and fits are similar. Included are (a) the total intensity S_0 for all values of electric field, (b) the total intensity S_0 for an expanded scale of electric fields near $E=0$, (c) the linear polarization S_1 for all values of electric field, and (d) the linear polarization S_1 for an expanded scale of electric fields near $E=0$.

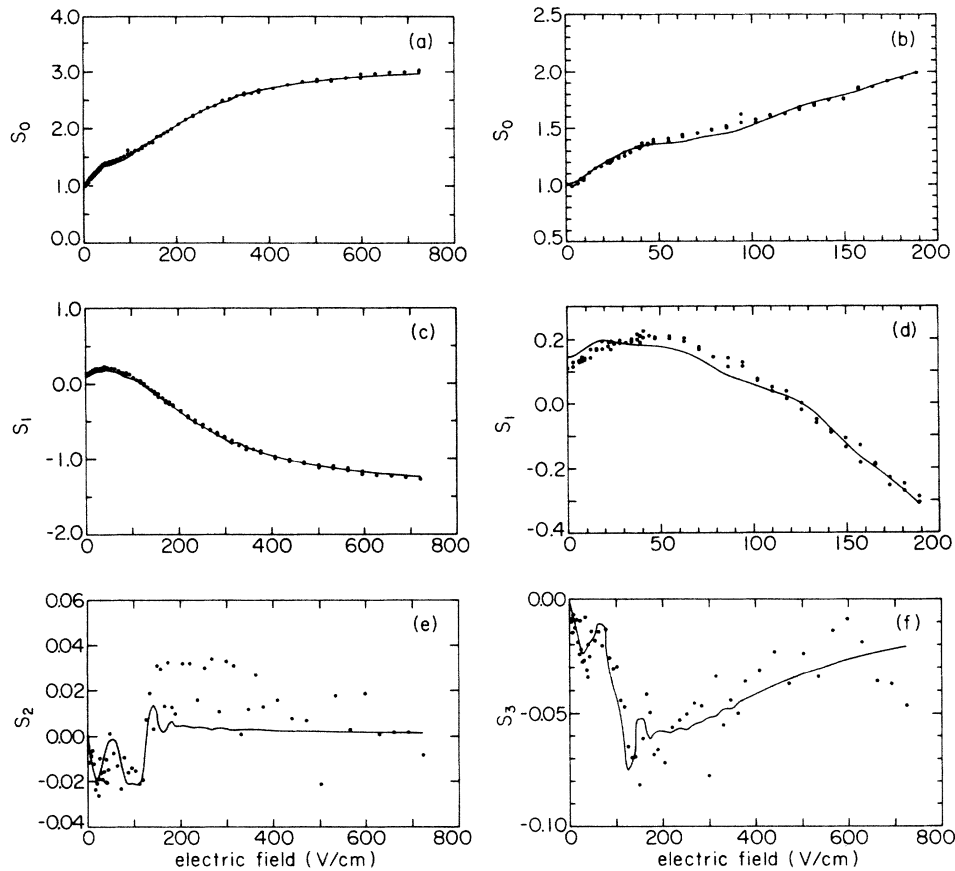


FIG. 12. Experimentally observed signals (data points) and fits (solid lines) to the signals for 60-keV $H^+ + He$ collision energy for transverse electric fields. The 40- and 80-keV data and fits are similar. Included are (a) the total intensity S_0 for all values of electric field, (b) the total intensity S_0 for an expanded scale of electric fields near $E=0$, (c) the linear polarization S_1 for all values of electric field, (d) the linear polarization S_1 for an expanded scale of electric fields near $E=0$, (e) the linear polarization S_2 at an angle of 45° for all values of electric field, and (f) the circular polarization S_3 for all values of electric field.

IV. RESULTS

A. Experimentally observed signals

As an example of this technique, the experimental data for the optical signals from 60-keV $H^+ + He$ collisions as a function of axial electric field are shown in Fig. 11. The data for transverse electric fields are shown in Fig. 12. Also shown in Figs. 11 and 12 are the fits to the experimental data which will be discussed below. The 40- and 80-keV data and fits are similar.

The six measured signals are normalized according to Eq. (2), i.e., the total intensity at zero electric field is equal to unity. The axial field data are shown for both directions of electric field. The transverse field data are shown only as a function of the magnitude of electric field since, as discussed in Sec. II, $S_0(E)$ and $S_1(E)$ were expected to be symmetric and $S_2(E)$ and $S_3(E)$ were expected to be antisymmetric in E . This expectation was realized for $S_0(E)$ and $S_1(E)$ since data for both polarities of electric field agreed to within the 1% statistical errors.

The statistical errors in the data points are approxi-

mately equal to the scatter in the points. More scatter is seen in $S_2(E)$ and $S_3(E)$ since these quantities were determined from the difference of two signals of approximately the same value.

The intensity and polarization signals show strong characteristic variations as a function of the applied electric fields. The increase in the total intensity signals $S_0(E)$ for both axial and transverse electric fields is caused by the relatively long lifetime for the $3s$ state which causes many of these atoms to decay after passing through the field of view of the detector. Application of the electric field mixes the $3s$ with the $3p$ and $3d$ states, shortening the lifetime (see Fig. 9) and causing more atoms to decay within the field of view so that the total intensity increases. In addition, the mixing of the $3p$ to the $3s$ and $3d$ states causes fewer atoms to decay by Lyman- β emission, increasing the Balmer- α signal. The linear polarization signals vary because of the selective sublevel mixing. The behavior of the linear polarization signals $S_1(E)$ is opposite for axial and transverse fields since the axial field mixes the $3s$ state to the $3p_0$ state and the transverse field mixes the $3s$ state to the $3p_{\pm 1}$ states. The circular polarization is induced by the transverse electric field.⁴⁹

B. Fits to the experimental observations

The fitted curves shown in Figs. 11 and 12 were produced by the density-matrix elements given in Table IV which are normalized so that $\rho_{s_0 s_0} = 1$. The elements are given in a representation in which the Condon and Shortley phase convention is used for the spherical harmonics (see, for example, Sec. 2.5 of Edmonds⁴²) and the radial functions are positive near the origin.

The fits to the first and second Stokes parameters, $S_0(E)$ and $S_1(E)$, respectively, are generally good for both the axial and transverse data. Some discrepancies exist near 25 V/cm for axial fields and near 40 V/cm for transverse fields. The fit to the fourth Stokes parameter $S_3(E)$ is generally good, particularly considering the large scatter in the data and the small values of the Stokes parameter which implied less weight in the fitting procedure.

The fit to the third Stokes parameter $S_2(E)$ for the transverse field data is not good. This poor fitting cannot be explained by the large scatter in the data and the small values of the parameter. A systematic error seems to be present in the fit of $S_2(E)$. Since the fits to the other five signals are significantly better than that for $S_2(E)$, the possibility of a systematic error in the experimental data is raised. This possibility is supported by the fact that an experimental check of the antisymmetry of $S_2(E)$ was not possible because of the method which was used to measure this parameter.

No error bars are given for the fitted density-matrix elements listed in Table IV. The fitting procedure generated error bars which reflect the ability of the fitting procedure to fit the experimental data with the calculated basis signals. Typical values for these error bars are ± 0.01 . How-

TABLE IV. Fitted density-matrix elements for collision energies of 40, 60, and 80 keV. The elements are normalized so that $\rho_{s_0 s_0} = 1$. Error bars are discussed in the text. The elements are given in a representation in which the hydrogen wave functions employ the Condon and Shortley phase convention for the spherical harmonics [see, for example, Sec. 2.5 of Edmonds (Ref. 42)] and the radial functions are positive near the origin.

Density-matrix element	Collision energy		
	40 keV	60 keV	80 keV
$\rho_{s_0 s_0}$	1.00	1.00	1.00
$\rho_{p_0 p_0}$	0.23	0.03	-0.09
$\rho_{p_{\pm 1} p_{\pm 1}}$	0.11	0.09	0.11
$\rho_{d_0 d_0}$	0.00	0.01	0.04
$\rho_{d_{\pm 1} d_{\pm 1}}$	0.06	0.04	0.03
$\rho_{d_{\pm 2} d_{\pm 2}}$	-0.01	-0.01	-0.01
$\text{Re}(\rho_{s_0 p_0})$	0.36	0.26	0.22
$\text{Re}(\rho_{s_0 d_0})$	0.18	0.17	0.18
$\text{Re}(\rho_{p_0 d_0})$	0.09	0.04	0.02
$\text{Re}(\rho_{p_{\pm 1} d_{\pm 1}})$	0.00	-0.01	0.00
$\text{Im}(\rho_{s_0 p_0})$	-0.26	-0.08	0.01
$\text{Im}(\rho_{s_0 d_0})$	-1.08	-0.80	-0.85
$\text{Im}(\rho_{p_0 d_0})$	0.00	-0.01	0.00
$\text{Im}(\rho_{p_{\pm 1} d_{\pm 1}})$	0.00	0.00	0.00

ever, these estimates do not take into account systematic uncertainties in the data or in the basis signals. In principle, the effect of these errors could be determined by changing the experimental data within the estimated uncertainties and then fitting this data with sets of basis signals which had been generated from models which took into account the possible sources of error. However, the cost in computer time of this procedure was prohibitive and error bars which include these uncertainties will not be given at this time. Also, it is believed that certain unknown experimental systematic errors exist in the data which cannot be determined without more extensive investigations. Thus, further analysis of the data is not warranted. New measurements are underway.

A check of the quality of the fit is given by the physical limitations on the values of the density-matrix elements, i.e., non-negative cross sections as indicated by Eq. (13) and bounded off-diagonal elements as indicated by Eq. (14). For each collision energy, the $d_{\pm 2}$ cross sections are negative but near 0. The p_0 cross section for 80-keV collision energy is negative by an amount far outside the error bar produced by the fitting procedure. This fact indicates that the errors introduced by the experimental data and/or the calculated basis signals are much larger than the error bars calculated by the fitting procedure. For the off-diagonal density-matrix elements, the magnitude of 8 of the 12 elements are outside the limits allowed by the corresponding diagonal terms. In particular, the imaginary parts of $\rho_{s_0 d_0}$ are far outside the limit, even when the fitting errors are taken into account. This fact reinforces the previous conclusion, i.e., the uncertainties in the density-matrix elements are much larger than the error bars determined by the fitting procedure. Thus, the results presented in Table IV should be taken only as an illustration of the technique and not as a measurement.

V. DISCUSSION

A. Physical interpretation of the density matrix

As stated above, the diagonal elements of the density matrix are proportional to the cross sections for producing the individual lm_l sublevels. The off-diagonal elements give the coherence or average phase difference between the two states. Additional significance of the density matrix is found when calculating the expectation value of different operators. For example, the expectation value of the z component of the electric dipole operator $\mathbf{d} = -e\mathbf{r}$ is given by the real parts of the off-diagonal density-matrix elements between states of opposite parity. (The symbol \mathbf{d} will be used for the electric dipole rather than the more common \mathbf{p} to avoid confusion with the linear momentum.) For the $n=3$ case considered here, $\langle d_z \rangle$ is given by

$$\langle d_z \rangle = \frac{6\sqrt{3}}{\text{Tr}(\rho^L)} \text{Re}(\sqrt{2}\rho_{s_0 p_0}^L + \rho_{p_0 d_0}^L + \sqrt{3}\rho_{p_1 d_1}^L) e a_0. \quad (36)$$

A similar interpretation for the imaginary parts of the off-diagonal density-matrix elements between states of opposite parity has also been sought in terms of the rate of change of the electric dipole.^{15,18,22,24,50} However, this in-

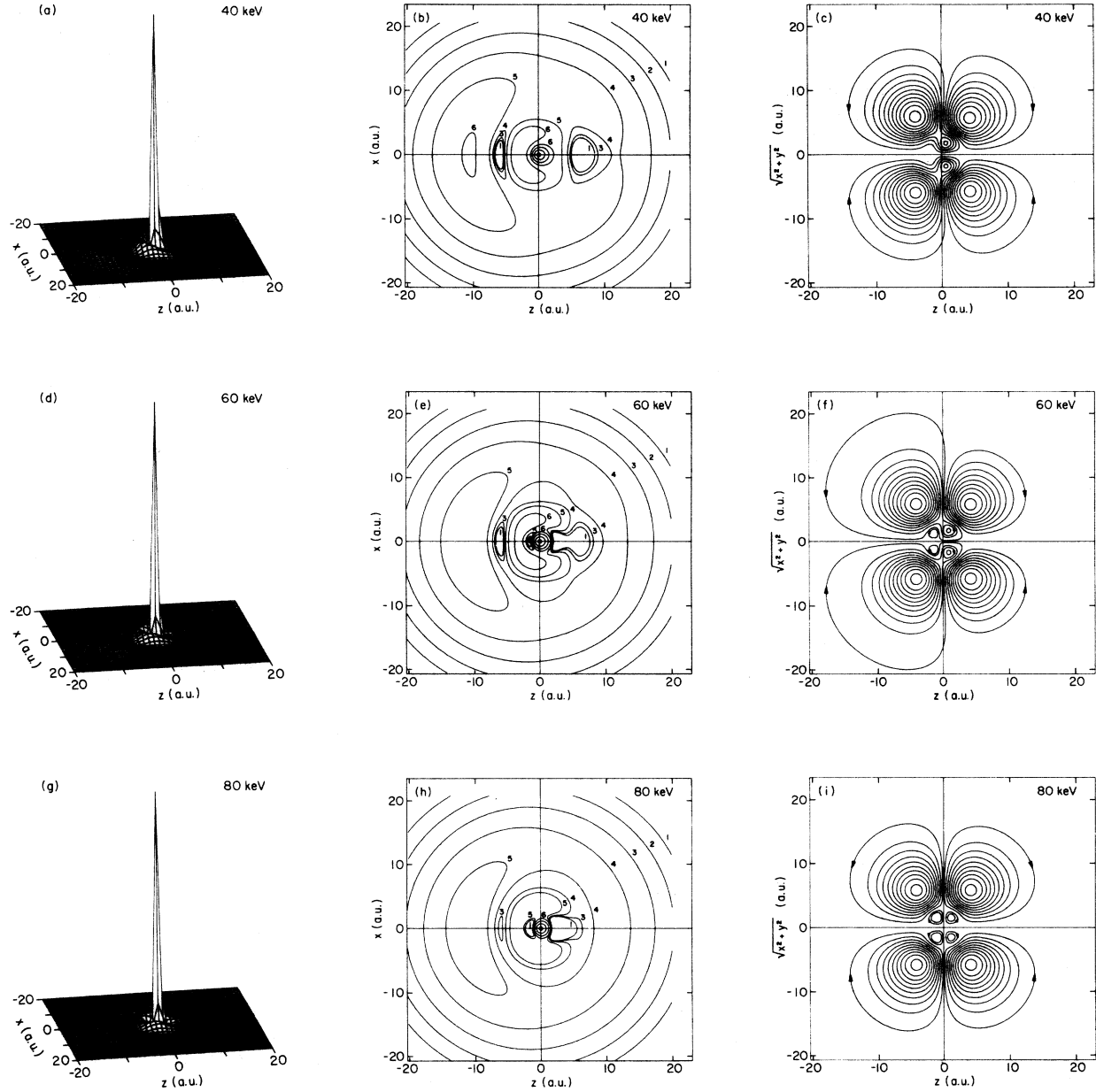


FIG. 13. Electron probability distribution and electron current distribution for $H(n=3)$ atoms formed in 40-, 60-, and 80-keV $H^+ + He$ collisions. Included are (a), (d), and (g), three-dimensional plots of the density distribution; (b), (e), and (h), contour plots of the density distribution; and (c), (f), and (i), current distributions for 40-, 60-, and 80-keV collision energies, respectively. For the probability density plots, the density in a plane containing the proton is plotted as a function of the z coordinate and the distance from the z axis $(x^2 + y^2)^{1/2}$. A logarithmic scale is used for the contour plots with each contour being labeled by the power p where the contours represent relative density levels of magnitude 3^p . For the electron current distributions, the flowlines separate equal flows weighted by the distance from the z axis, i.e., equal amounts of $(x^2 + y^2)^{1/2}j$.

terpretation is unsatisfactory^{17,25,26} since it depends on the small relativistic and quantum electrodynamic energy splittings and loses meaning when applied to a nonrelativistic hydrogen atom.

Burgdörfer²⁷ has provided an explicit parametrization for the hydrogen-atom density matrix by showing that any n -shell density matrix may be expressed in terms of operators constructed from the angular momentum \mathbf{L} and the Runge-Lenz vector \mathbf{A} ,

$$\mathbf{A} = \frac{1}{\sqrt{-2mE}} \left[\frac{1}{2}(\mathbf{p} \times \mathbf{L} - \mathbf{L} \times \mathbf{p}) - me^2 \hat{\mathbf{r}} \right], \quad (37)$$

where E is the energy of the shell considered, m is the electron mass, e is the electron charge, \mathbf{p} is the linear momentum, and \mathbf{r} is the position. For a classical Kepler orbit, \mathbf{A} is proportional to the eccentricity and points toward the perihelion of the orbit. Burgdörfer and Dubé²⁸ have applied the classical interpretation for \mathbf{A} to the re-

sults of their calculations of the density matrix describing hydrogen atoms produced in the $H^+ + He$ collision studied in this paper. Their interpretation suggests that the elliptical orbit of the collisionally produced hydrogen atom is displaced behind the proton and is tilted with respect to the collision axis. This approach is limited, however, because it relies on the classical interpretation of \mathbf{A} .

An alternative interpretation³ for the density matrix is provided by the electron probability density $D(\mathbf{r})$ and the electron current distribution $\mathbf{j}(\mathbf{r})$,

$$D(\mathbf{r}) = \sum_{l, m_l, l', m_l'} \text{Re}[\rho_{lm_l, l'm_l'}^L \psi_{3l'm_l'}^*(\mathbf{r}) \psi_{3lm_l}(\mathbf{r})] \quad (38)$$

and

$$\mathbf{j}(\mathbf{r}) = \sum_{l, m_l, l', m_l'} \text{Im}[\rho_{lm_l, l'm_l'}^L \psi_{3l'm_l'}^*(\mathbf{r}) \nabla \psi_{3lm_l}(\mathbf{r})]. \quad (39)$$

Thus $D(\mathbf{r})$ and $\mathbf{j}(\mathbf{r})$ provide a physical interpretation in which each of the independent elements of the density matrix contribute. For the axially symmetric collision studied in this report, Eqs. (10)–(12) imply that the electron current distribution is determined by the imaginary parts of the off-diagonal density-matrix elements. The real parts of these elements, along with the diagonal elements, give the density distribution.

B. Results from the fitted density matrices

Figure 13 shows three-dimensional and contour plots of $D(\mathbf{r})$ and a flow pattern for $\mathbf{j}(\mathbf{r})$ for the $H(n=3)$ atoms described by the density matrices given in Table IV. The probability density plots are dominated by a large peak centered at the position of the proton which is produced by the $3s$ component of the probability distribution. Surrounding the peak are two ridges produced by the remaining density-matrix elements. These ridges are asymmetric in the forward and backward hemisphere because of the contributions from the off-diagonal density-matrix elements between states of opposite parity which give rise to an electric dipole moment according to Eq. (36). The value of the electric dipole moment calculated from the density-matrix elements listed in Table IV is plotted as a function of collision energy in Fig. 14. The dipole moment shown in Fig. 14 is large, reaching $4.0ea_0$ at 40-keV collision energy. This value should be compared to $7.3ea_0$, the maximum allowed within the $n=3$ manifold.

A quantitative measure of the electron current distribution is provided by the quantity $\langle (\mathbf{A} \times \mathbf{L})_z \rangle_s$, which is given by

$$\begin{aligned} \langle (\mathbf{A} \times \mathbf{L})_z \rangle_s &= \frac{1}{2} \langle (\mathbf{A} \times \mathbf{L} - \mathbf{L} \times \mathbf{A})_z \rangle \\ &= \frac{-8}{\text{Tr}(\rho^L)} \left[\frac{2}{3} \right]^{1/2} \text{Im}(\rho_{s_0 p_0}^L + \sqrt{2} \rho_{p_0 d_0}^L \\ &\quad + \sqrt{6} \rho_{p_1 d_1}^L) \hbar^2. \end{aligned} \quad (40)$$

The value of $\langle (\mathbf{A} \times \mathbf{L})_z \rangle_s$, calculated from the density-matrix elements listed in Table IV is plotted as a function

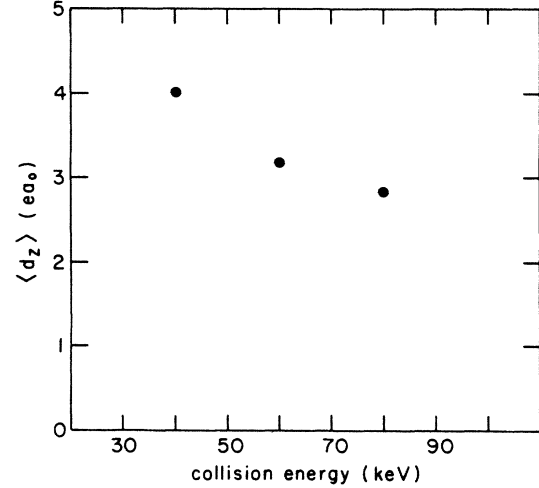


FIG. 14. Electric dipole moment $\langle d_z \rangle$ vs collision energy.

of the collision energy in Fig. 15. The quantity $\langle (\mathbf{A} \times \mathbf{L})_z \rangle_s$ is a measure of the z component of the current, weighted so that the outer portion of the distribution contributes more than the inner portion. The current plots in Fig. 13 suggest that $\langle (\mathbf{A} \times \mathbf{L})_z \rangle_s$ is negative for the cases of 40- and 60-keV collision energy and is approximately zero for the case of 80-keV collision energy, in agreement with Fig. 15.

The flow patterns of the electron current distribution for the three collision energies are similar since each is dominated by the contribution from the imaginary part of the $\rho_{s_0 d_0}$ term. Since the magnitude of this term is outside the limit allowed by the diagonal $\rho_{s_0 s_0}$ and $\rho_{d_0 d_0}$ terms for each of the three collision energies, the accuracy of the current pattern is difficult to determine. The current patterns presented in Fig. 13 are qualitatively different from the pattern given in Ref. 3 since the values of some of the density-matrix elements used to produce the pattern in Ref. 3 were selected from a fit to the transverse electric field data only. This procedure was followed since the magnitude of the obtained density-matrix elements were within the physical limitation expressed by Eq. (14). Thus

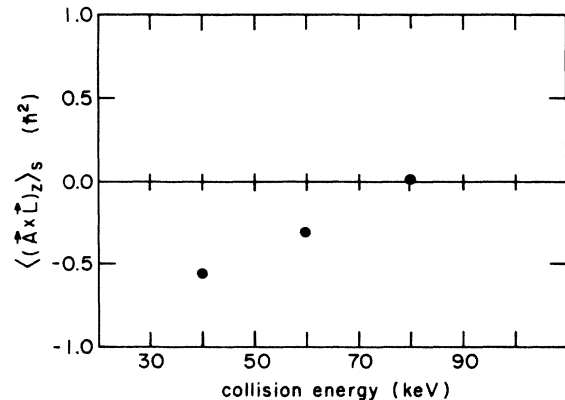


FIG. 15. $\langle (\mathbf{A} \times \mathbf{L})_z \rangle_s$ vs collision energy.

the current distribution of Ref. 3 is probably more realistic, but the patterns presented here are representative of the density matrices given in Table IV. The values of the quantity $\langle (\mathbf{A} \times \mathbf{L})_z \rangle_s$ plotted in Fig. 15 do not include contributions from the imaginary part of $\rho_{s_0 d_0}$ and should, therefore, be more meaningful than the electron current distribution.

VI. CONCLUSION

This paper presents an experimental technique and analysis procedure for determining the density matrix for collisionally produced $\text{H}(n=3)$ atoms. The density matrix gives the most complete description of the collisionally produced atoms including the cross sections for producing individual sublevels and coherences between sublevels. In particular, the coherence terms show that an electric dipole moment and electron current distribution are induced in the atoms. These physically meaningful quantities provide valuable information concerning the dynamics of the electron-transfer process.

The technique used to measure the density matrix has many attractive features. The applied electric fields are insufficient to affect the collision process but modify the subsequent time evolution in a well-understood manner. Since the fields are applied in the collision cell and the optical system views radiation emitted from within the col-

lision cell, no "turn on" or "turn off" effects are present. Since the optical system averages over several quantum-beat cycles and because atoms are formed throughout the collision cell, the experimental signals are not sensitive to the relative positioning of the detector with respect to the collision cell.

Because of imperfections in the present experiment most of the elements in the density matrix have not been determined accurately. Some of the possible systematic errors which can affect the determination of the density matrix include residual polarization sensitivity of the photomultiplier tube, fringing field effects for the transverse electric field, energy dependence of the fitting functions, and, most importantly, cascade effects. Because of the importance in atomic collision physics of determining the density matrix for $\text{H}^+ + \text{He}$ collisions, future applications of the technique described in this paper need to pay careful attention to eliminating these systematic uncertainties.

ACKNOWLEDGMENTS

The authors would like to thank J. Macek, J. Burgdörfer, N. H. Tolk, and J. C. Tully for helpful discussions. This work was supported in part by the Atomic, Molecular, and Plasma Physics Program of the National Science Foundation, under Grant No. PHY-82-8905.

APPENDIX A: MATRIX ELEMENTS OF THE STARK INTERACTION

Matrix elements of the Stark interaction $e\mathbf{r} \cdot \mathbf{E}$ in the (l, s, j, m_j) representation are

$$\langle l s j m_j | e\mathbf{r} \cdot \mathbf{E} | l' s' j' m_j' \rangle = e \sum_q (-1)^q E_{-q} \langle l s j m_j | r_q | l' s' j' m_j' \rangle, \quad (\text{A1})$$

where r_σ and E_σ are the spherical components of \mathbf{r} and \mathbf{E} [see, for example, Eq. (5.1.3) of Edmonds⁴²]. The matrix elements of r_q were evaluated in the (l, m_l, s, m_s) representation and transformed to the (l, s, j, m_j) representation,

$$\langle l s j m_j | r_q | l' s' j' m_j' \rangle = \sum_{\substack{m_l, m_l' \\ m_s, m_s'}} \langle l s j m_j | l m_l s m_s \rangle \langle l m_l s m_s | r_q | l' m_l' s' m_s' \rangle \langle l' m_l' s' m_s' | l' s' j' m_j' \rangle. \quad (\text{A2})$$

The matrix element of r_q on the right-hand side of Eq. (A2) may be written as

$$\langle l m_l s m_s | r_q | l' m_l' s' m_s' \rangle = \langle l m_l | r_q | l' m_l' \rangle \delta_{m_s m_s'}. \quad (\text{A3})$$

Expressing the first and third terms on the right-hand side of Eq. (A2) in terms of 3- j symbols [see, for example, Eq. (3.7.3) of Edmonds⁴²] and using the Wigner-Eckart theorem [see, for example, Eq. (5.4.1) of Edmonds⁴²] to factor the matrix element on the right-hand side of Eq. (A3) gives

$$\begin{aligned} \langle l s j m_j | r_q | l' s' j' m_j' \rangle &= \sqrt{(2j+1)(2j'+1)} \langle l || \mathbf{r} || l' \rangle \\ &\times \sum_{\substack{m_l, m_l' \\ m_s}} \left\{ (-1)^{l+s+m_j+l+m_l+l'+s+m_j'} \begin{bmatrix} l & s & j \\ m_l & m_s & -m_j \end{bmatrix} \begin{bmatrix} l & 1 & l' \\ -m_l & q & m_l' \end{bmatrix} \begin{bmatrix} l' & s & j' \\ m_l' & m_s & -m_j' \end{bmatrix} \right\}, \end{aligned} \quad (\text{A4})$$

where the sum over m'_s has been performed. Using the symmetry properties of the 3- j symbols [see, for example, Eq. (3.7.5) of Edmonds⁴²] and using Eq. (6.2.8) of Edmonds,⁴² Eq. (A4) may be written as

$$\begin{aligned} & \langle l s j m_j | r_q | l' s' j' m'_j \rangle \\ &= (-1)^{l+s-m_j} \sqrt{(2j+1)(2j'+1)} \langle l || r || l' \rangle \\ & \times \begin{Bmatrix} j' & 1 & j \\ m'_j & q & -m_j \end{Bmatrix} \begin{Bmatrix} j' & 1 & j \\ l & s & l' \end{Bmatrix}. \end{aligned} \quad (\text{A5})$$

Combining Eqs. (A5) and (A1) gives Eq. (20).

APPENDIX B: EXPRESSION FOR THE POLARIZATION TENSOR \vec{C}

Comparing Eqs. (32) and (33), it is seen that the polarization tensor \vec{C} may be written as

$$\begin{aligned} \vec{C} &= \frac{e^2 \omega^3}{2\pi \hbar c^3} \sum_{\substack{(l, m_l), (l', m_{l'}) \\ (l_f, m_{l_f})}} \langle l_f m_{l_f} | r | l m_l \rangle \tilde{\rho}_{l m_l, l' m_{l'}}^L \\ & \times \langle l' m_{l'} | r | l_f m_{l_f} \rangle. \end{aligned} \quad (\text{B1})$$

Expressing the vectors r in Eq. (B1) in terms of their spherical components [see, for example, Eq. (5.1.3) of Edmonds⁴²], \vec{C} may be written as

$$\begin{aligned} \vec{C} &= \frac{e^2 \omega^3}{2\pi \hbar c^3} \sum_{\substack{k, q, \sigma, \sigma', \\ l, l', l_f}} \left\{ (-1)^{\sigma} \hat{e}_{\sigma} \hat{e}_{\sigma'}^* \sqrt{2k+1} \langle l_f || r || l \rangle \langle l' || r || l_f \rangle \tilde{\rho}_{kq}^L(l, l') \right. \\ & \times \sum_{\substack{m_l, m_{l'}, \\ m_{l_f}}} \left. \left((-1)^{l_f+2l'-m_{l_f}-2m_l} \begin{Bmatrix} l_f & 1 & l \\ -m_{l_f} & -\sigma & m_l \end{Bmatrix} \begin{Bmatrix} l' & k & l \\ -m_{l'} & q & m_l \end{Bmatrix} \begin{Bmatrix} l' & 1 & l_f \\ -m_{l'} & \sigma' & m_{l_f} \end{Bmatrix} \right) \right\}. \end{aligned} \quad (\text{B7})$$

Using the symmetry properties of the 3- j symbols [see, for example, Eq. (3.7.5) of Edmonds⁴²] and using Eq. (6.2.8) of Edmonds,⁴² \vec{C} may be written as

$$\vec{C} = \sum_{k, q} c_{kq} \vec{S}_{kq}^{\dagger}, \quad (\text{B8})$$

where

$$\begin{aligned} c_{kq} &= \frac{e^2 \omega^3}{2\pi \hbar c^3} \sum_{l, l', l_f} (-1)^{l+l'+k+1} \langle l_f || r || l \rangle \langle l' || r || l_f \rangle \\ & \times \tilde{\rho}_{kq}^L(l, l') \begin{Bmatrix} 1 & k & 1 \\ l & l_f & l' \end{Bmatrix} \end{aligned} \quad (\text{B9})$$

$$\begin{aligned} \vec{C} &= \frac{e^2 \omega^3}{2\pi \hbar c^3} \sum_{\sigma, \sigma'} (-1)^{\sigma} \hat{e}_{\sigma} \hat{e}_{\sigma'}^* \\ & \times \sum_{\substack{l, m_l, l', m_{l'} \\ l_f, m_{l_f}}} \langle l_f m_{l_f} | r_{-\sigma} | l m_l \rangle \tilde{\rho}_{l m_l, l' m_{l'}}^L \\ & \times \langle l' m_{l'} | r_{\sigma'} | l_f m_{l_f} \rangle, \end{aligned} \quad (\text{B2})$$

where the spherical unit vectors are given by

$$\hat{e}_0 = \hat{e}_z \quad \text{and} \quad \hat{e}_{\pm 1} = \mp \frac{1}{\sqrt{2}} (\hat{e}_x \pm i \hat{e}_y). \quad (\text{B3})$$

The integrated density matrix $\tilde{\rho}^L$ may be expanded in a complete set of tensor operators $T_{kq}(l, l')$,

$$\tilde{\rho}^L = \sum_{\substack{k, q \\ l, l'}} \tilde{\rho}_{kq}^L(l, l') T_{kq}^{\dagger}(l, l'), \quad (\text{B4})$$

where matrix elements of the $T_{kq}(l, l')$ are

$$\begin{aligned} & \langle l m_l | T_{kq}(l, l') | l' m_{l'} \rangle \\ &= (-1)^{l-m_l} \sqrt{2k+1} \begin{Bmatrix} l & k & l' \\ -m_l & q & m_{l'} \end{Bmatrix}. \end{aligned} \quad (\text{B5})$$

The expansion coefficients in Eq. (B4) are

$$\tilde{\rho}_{kq}^L(l, l') = \text{Tr}[\tilde{\rho}^L T_{kq}(l, l')]. \quad (\text{B6})$$

Applying the Wigner-Eckart theorem [see, for example, Eq. (5.4.1) of Edmonds⁴²] to the first and third matrix elements on the right-hand side in Eq. (B2) and using Eqs. (B4) and (B5), \vec{C} may be written as

and where the \vec{S}_{kq} form an orthonormal set of 3×3 basis tensors and are given by

$$\vec{S}_{kq} = \sum_{\sigma, \sigma'} \hat{e}_{\sigma} (-1)^{k+\sigma+1} \sqrt{2k+1} \begin{Bmatrix} 1 & k & 1 \\ \sigma' & q & -\sigma \end{Bmatrix} \hat{e}_{\sigma'}^*. \quad (\text{B10})$$

Explicit expressions for the \vec{S}_{kq} are given by Carrington.⁵¹

- *Present address: Oak Ridge National Laboratory, Oak Ridge, TN 37831.
- †Permanent address: Department of Physics, Hope College, Holland, MI 49423.
- ¹C. C. Havener, W. B. Westerveld, J. S. Risley, N. H. Tolk, and J. C. Tully, *Phys. Rev. Lett.* **48**, 926 (1982).
- ²C. C. Havener, Ph.D. thesis, North Carolina State University, 1983.
- ³C. C. Havener, N. Rouze, W. B. Westerveld, and J. S. Risley, *Phys. Rev. Lett.* **53**, 1049 (1984).
- ⁴J. E. Bayfield, in *Atomic Physics*, edited by G. zu Putnitz, E. W. Weber, and A. Winnacker (Plenum, New York, 1975), Vol. 4, p. 397.
- ⁵E. W. Thomas, *Excitation in Heavy Particle Collisions* (Wiley, New York, 1972).
- ⁶R. H. Hughes, C. A. Stigers, B. M. Doughty, and E. D. Stokes, *Phys. Rev. A* **1**, 1424 (1970).
- ⁷M. C. Brower and F. M. Pipkin, *Bull. Am. Phys. Soc.* **29**, 816 (1984).
- ⁸R. J. Knize, S. R. Lundeen, and F. M. Pipkin, *Phys. Rev. Lett.* **49**, 315 (1982).
- ⁹H. G. Berry and M. Hass, in *Annual Review of Nuclear and Particle Science*, edited by J. D. Jackson, H. E. Gore, and R. F. Schwitters (Annual Reviews, Palo Alto, 1982), p. 1.
- ¹⁰D. J. Burns and W. H. Hancock, *Phys. Rev. Lett.* **27**, 370 (1971).
- ¹¹A. Denis, J. Desesquelles, M. Druetta, and M. Dufay, in *Beam Foil Spectroscopy*, edited by I. A. Sellin and D. J. Pegg (Plenum, New York, 1976), p. 799.
- ¹²J. Carmeliet, J. C. Dehaes, and W. Singer, *J. Phys. (Paris) Colloq.* **40**, C1-335 (1979).
- ¹³J. C. Dehaes and W. Singer, *Phys. Lett.* **75A**, 276 (1980).
- ¹⁴T. G. Eck, *Phys. Rev. Lett.* **31**, 270 (1973).
- ¹⁵I. A. Sellin, J. R. Mowat, R. S. Peterson, P. M. Griffin, R. Laubert, and H. H. Haselton, *Phys. Rev. Lett.* **31**, 1335 (1973).
- ¹⁶A. Gaupp, H. J. Andrä, and J. Macek, *Phys. Rev. Lett.* **32**, 268 (1974).
- ¹⁷G. Gabrielse, *Phys. Rev. A* **23**, 775 (1981).
- ¹⁸I. A. Sellin, L. Liljebj, S. Mannervik, and S. Hultberg, *Phys. Rev. Lett.* **26**, 570 (1979).
- ¹⁹M. Lombardi and M. Giroud, *Phys. Rev. Lett.* **36**, 409 (1976).
- ²⁰A. H. Mahan and S. J. Smith, *Phys. Rev. A* **16**, 1789 (1977).
- ²¹R. Krotkov, *Phys. Rev. A* **12**, 1793 (1975).
- ²²R. Krotkov and J. Stone, *Phys. Rev. A* **22**, 473 (1980).
- ²³U. Fano and J. H. Macek, *Rev. Mod. Phys.* **45**, 553 (1973).
- ²⁴G. Gabrielse and Y. B. Band, *Phys. Rev. Lett.* **39**, 697 (1977).
- ²⁵Y. B. Band, *Phys. Rev. A* **19**, 1906 (1979).
- ²⁶G. Gabrielse, *Phys. Rev. A* **22**, 138 (1980).
- ²⁷J. Burgdörfer, *Z. Phys. A* **309**, 285 (1983).
- ²⁸J. Burgdörfer and L. J. Dubé, *Phys. Rev. Lett.* **52**, 2225 (1984).
- ²⁹G. G. Stokes, *Trans. Cambridge Philos. Soc.* **9**, 399 (1852).
- ³⁰M. Born and E. Wolf, *Principles of Optics*, 6th ed. (Pergamon, Oxford, 1980).
- ³¹F. Mooney, *J. Opt. Soc.* **42**, 181 (1952).
- ³²K. Blum, *Density Matrix Theory and Applications* (Plenum, New York, 1981).
- ³³M. T. Grisaru, H. N. Pendleton, and R. Petraso, *Ann. Phys. (N.Y.)* **79**, 518 (1973).
- ³⁴H. K. Holt and I. A. Sellin, *Phys. Rev. A* **6**, 508 (1972).
- ³⁵E. J. Kelsey and J. Macek, *Phys. Rev. A* **16**, 1322 (1977).
- ³⁶F. E. Low, *Phys. Rev. A* **20**, 1567 (1979).
- ³⁷M. Hillery and P. J. Mohr, *Phys. Rev. A* **21**, 24 (1980).
- ³⁸L. P. Lévy, *Phys. Rev. A* **29**, 3189 (1984).
- ³⁹J. S. Risley, F. J. de Heer, and C. B. Kerkijk, *J. Phys. B* **11**, 1759 (1978).
- ⁴⁰H. A. Bethe and E. E. Salpeter, *Quantum Mechanics of One- and Two-Electron Atoms* (Plenum, New York, 1977).
- ⁴¹R. H. Hughes, H. R. Dawson, and B. M. Doughty, *Phys. Rev.* **164**, 166 (1967).
- ⁴²A. R. Edmonds, *Angular Momentum in Quantum Mechanics* (Princeton University, Princeton, N.J., 1974).
- ⁴³Computer code EIGCC, IMSL Library, 9th ed. (IMSL, Inc., Houston, TX) 1982.
- ⁴⁴G. Lüders, *Ann. Phys. (Leipzig)* **8**, 301 (1951).
- ⁴⁵G. Nienhuis, in *Coherence and Correlation in Atomic Collisions*, edited by H. Kleinpoppen and J. F. Williams (Plenum, New York, 1980), p. 121.
- ⁴⁶N. H. Tolk and J. C. Tully (private communication).
- ⁴⁷Computer code GLM, SAS User's Guide (SAS Institute, Inc., Cary, NC) 1982.
- ⁴⁸S. L. Meyer, *Data Analysis for Scientists and Engineers* (Wiley, New York, 1975).
- ⁴⁹M. Lombardi, M. Giroud, and J. Macek, *Phys. Rev. A* **11**, 1114 (1975).
- ⁵⁰A. Denis, J. Desesquelles, M. Druetta, and D. J. Pegg, *Nucl. Instrum. Methods* **194**, 363 (1982).
- ⁵¹C. G. Carrington, *J. Phys. B* **4**, 1222 (1971).

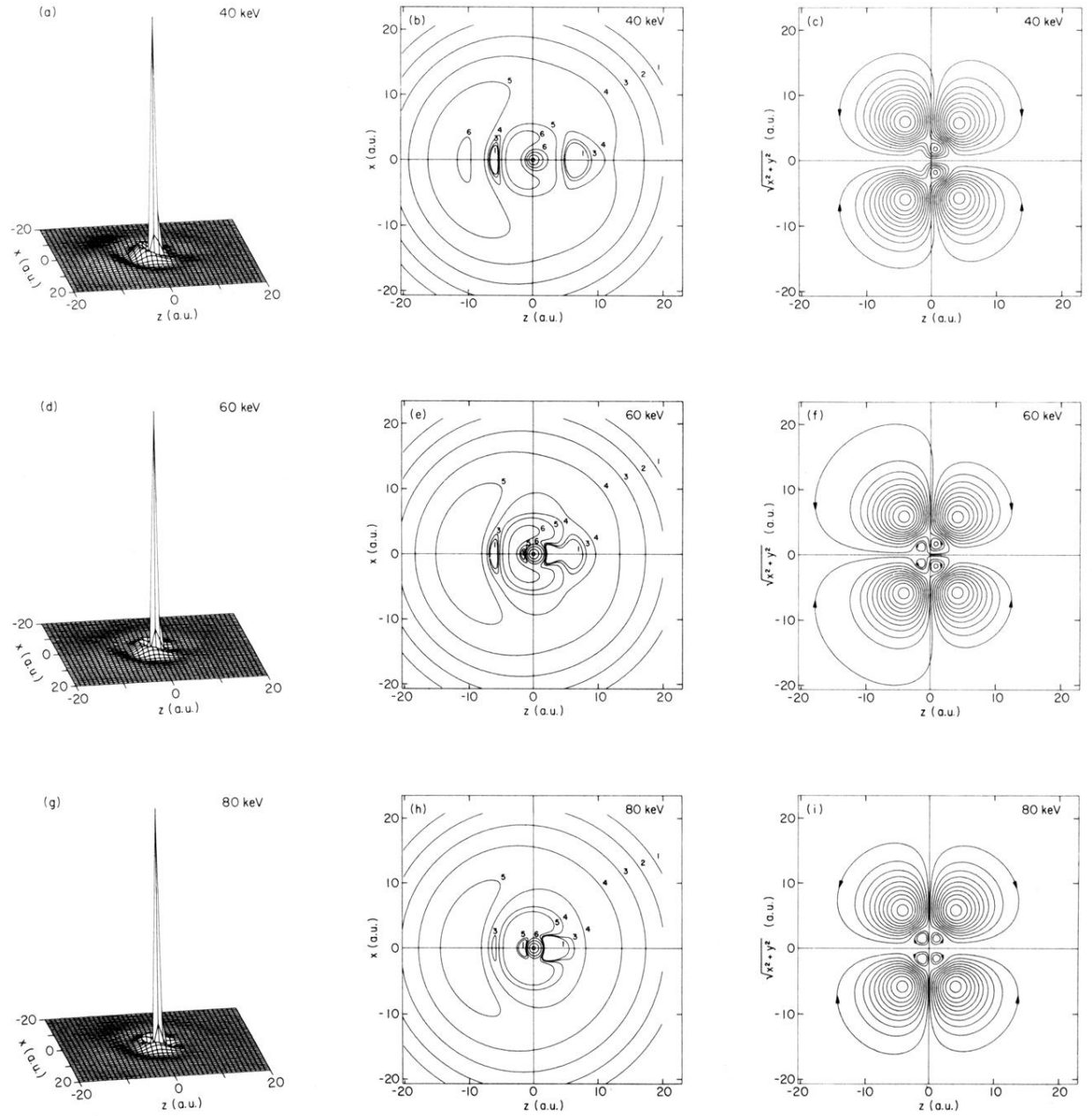


FIG. 13. Electron probability distribution and electron current distribution for $H(n=3)$ atoms formed in 40-, 60-, and 80-keV $H^+ + He$ collisions. Included are (a), (d), and (g), three-dimensional plots of the density distribution; (b), (e), and (h), contour plots of the density distribution; and (c), (f), and (i), current distributions for 40-, 60-, and 80-keV collision energies, respectively. For the probability density plots, the density in a plane containing the proton is plotted as a function of the z coordinate and the distance from the z axis $(x^2 + y^2)^{1/2}$. A logarithmic scale is used for the contour plots with each contour being labeled by the power p where the contours represent relative density levels of magnitude 3^p . For the electron current distributions, the flowlines separate equal flows weighted by the distance from the z axis, i.e., equal amounts of $(x^2 + y^2)^{1/2}j$.